Table 1. Twelve months of *H. pylori* infection increases the mutation frequency of A:T-to-G:C transitions and G:C-to-T:A transversions in female mice

	6 mo			12 mo		
Effect	Uninfected all (n = 6)	Infected male (n = 4)	Infected female (n = 8)	Uninfected all (n = 14)	Infected male (n = 5)	Infected female (n = 11)
Transition						
G:C to A:T	3.02 (2.07)	2.41 (2.64)	2.74 (1.07)	2.13 (0.87)	2.66 (1.70)	2.69 (0.97)
A:T to G:C	0.27 (0.61)	0.00	0.16 (0.22)	0.23 (0.19)	0.08 (0.16)	0.88 (0.59)*
Transversion						
G:C to T:A	1.30 (1.34)	1.64 (1.29)	0.89 (0.68)	0.85 (0.62)	1.69 (2.43)	1.75 (0.54)*
G:C to C:G	0.29 (0.66)	0.36 (0.71)	0.40 (0.60)	0.19 (0.27)	0.84 (1.25)	0.09 (0.14)
A:T to T:A	0.34 (0.47)	0.00	0.37 (0.37)	0.31 (0.41)	0.00	0.53 (0.89)
A:T to C:G	0.00	0.36 (0.71)	0.18 (0.22)	0.05 (0.12)	0.00	0.25 (0.46)
Deletion						
1-bp deletion	0.84 (0.94)	2.44 (3.99)	0.66 (0.43)	0.53 (0.35)	0.67 (0.54)	0.88 (0.73)
≥2-bp deletion	0.04 (0.12)	0.00	0.44 (0.57)	0.22 (0.20)	0.18 (0.36)	0.22 (0.34)
Insertion	0.00	0.00	0.08 (0.16)	0.20 (0.23)	0.00	0.11 (0.17)
Complex mutation	0.14 (0.31)	0.00	0.04 (0.08)	0.00	0.18 (0.36)	0.12 (0.29)
Total	6.23 (2.98)	7.20 (2.21)	5.95 (1.54)	4.71 (1.13)	6.29 (5.37)	7.51 (1.91)*

Data are mean (SD) of mutation frequency data from 411 mutants recovered from the *gpt* assay after excluding 155 mutants considered siblings. Control mice of both sexes were grouped for this analysis. The mutation frequency of A:T-to-G:C transitions and G:C-to-T:A transversions was significantly elevated in female mice infected with *H. pylori* for 12 mo.
*$P < 0.05$.

Mutation analysis using the Spi⁻ assay revealed that the frequency of deletion mutations in *gpt* of gastric tissue DNA was not significantly affected by *H. pylori* infection (Fig. 5). Analyses of 57 samples from 32 mice showed that Spi⁻ mutant frequencies in infected mice (females at 6 MPI, $4.8 \pm 2.5 \times 10^{-6}$, $P = 0.09$; females at 12 MPI, $5.0 \pm 2.6 \times 10^{-6}$, $P = 0.30$; males at 6 MPI, $6.3 \pm 2.5 \times 10^{-6}$, $P = 0.87$; and males at 12 MPI, $5.2 \pm 1.4 \times 10^{-6}$, $P = 0.17$) were not significantly different from those of age-matched controls at either time point (all mice at 6 MPI, $2.9 \pm 1.3 \times 10^{-6}$; all mice at 12 MPI, $3.6 \pm 1.8 \times 10^{-6}$).

Current models of inflammation-driven carcinogenesis are based on chronic inflammation inducing mutations that lead to cancer (40, 41). Female mice at 6 MPI had more hyperplasia, epithelial defects, and dysplasia than infected males and age-matched controls, but this increase in pathologic findings was not accompanied by increased frequency of mutations. This was detected only in infected female mice at 12 MPI, which had experienced more severe gastritis for a longer period, suggesting
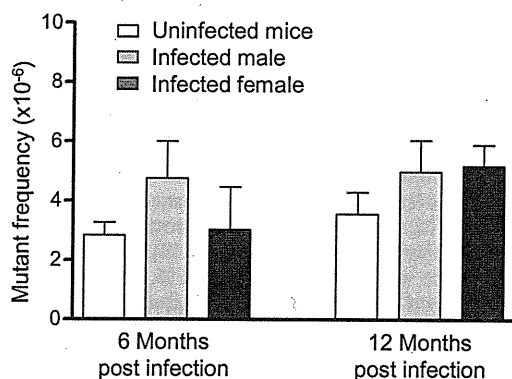

Fig. 5. Mutant frequency of deletions was unchanged by *H. pylori* infection. *H. pylori* infection did not alter the levels of deletions detected by the Spi⁻ assay in uninfected mice (white bars; 6 MPI, n = 12; 12 MPI, n = 16), *H. pylori*-infected males (light gray bars; 6 MPI, n = 3; 12 MPI, n = 5) and *H. pylori*-infected females (dark gray bars; 6 MPI, n = 9; 12 MPI, n = 12). Control mice of both sexes were grouped for this analysis. Data are mean (SEM) of mutant frequency of mice in different treatment groups.

that gastritis is necessary but not sufficient to induce mutagenesis. Similarly, duration of infection in itself was insufficient, as mutation frequency was not increased in male mice at 12 MPI. Based on the GHAI, infected male mice had a weaker response at 6 MPI compared with infected females, whereas by 12 MPI, the level of pathologic process was similar in both sexes. These data suggest that the delayed onset of severe gastric lesions in males reduced the duration of their exposure to chronic gastritis, protecting them from mutagenesis, highlighting the importance of severity and duration of the inflammatory response.

Our findings agree with current paradigms for the role of inflammation in carcinogenesis (4) and with the more severe pathology induced in female versus male C57BL/6 mice infected with *Helicobacter* spp. (42). Our observations in female *gpt* delta mice are consistent with previously reported data from female C57BL/6 Big Blue mice infected with *H. felis*, which induces more severe gastritis at earlier time points than *H. pylori*, effectively increasing the amount of DNA damage inflicted after infection (23, 43, 44). The higher mutation frequency found at 7 MPI in *H. felis*-infected female C57BL/6 Big Blue mice may be comparable to that occurring at 12 MPI in female *gpt* delta mice infected with *H. pylori*, based on increased inflammation and epithelial proliferation. In contrast, another study of DNA point mutations induced by *H. pylori* in male Big Blue mice reported that, although mutant frequency was increased at 6 MPI, it returned to control levels by 12 MPI (22). The decrease between 6 and 12 MPI was accompanied by loss of *iNOS* expression and reversion of the mutation spectrum to one indistinguishable from that of uninfected mice (22). Two possible explanations for these results are that (*i*) the increase in mutations at 6 MPI may have reflected jackpot mutations, because clonal expansion was not assessed or (*ii*) loss of infection resulted in absence of iNOS expression and reversion of the mutation spectrum. An additional factor pertinent to comparisons of previous mutagenesis studies involving gastric infection by *Helicobacter* spp. is the endogenous *Helicobacter* status of the mouse colony (45). We recently reported that concurrent, subclinical infection in C57BL/6 mice with nongastric *Helicobacter bilis* significantly reduced *H. pylori*-associated premalignant gastric lesions at 6 and 11 MPI (46). This immunomodulatory effect could affect observed mutagenic responses,

and it is unknown whether Big Blue mice used in previous studies were free of enteric *Helicobacter* spp.

Our observed sex-based effects on mutagenesis induced by *H. pylori* in mice has not been reported previously, but sex bias has been found in other responses to infection. In *H. pylori*–infected Mongolian gerbils, immune responses and cytokine production were reported to be affected by sex (47), and *H. pylori* preferentially induced cancer in male INS-GAS mice (48). Greater female susceptibility to gastric *Helicobacter* infections has been noted previously in WT C57BL/6 mice (42), whereby females infected with *H. felis* experience an earlier onset of gastric inflammation, epithelial hyperplasia, atrophy, and apoptosis (42). Mechanisms responsible for the observed sex-based effects are incompletely understood, but findings to date collectively indicate that sex is an important variable, affecting strength of the host response to *H. pylori* infection, which in turn determines disease outcome.

The typical host response to *Helicobacter* infection is a proinflammatory Th1 response that causes chronic gastritis (49, 50). However, mouse strains such as BALB/c, which mount a strong antiinflammatory Th2 humoral immune response to *H. pylori* infection, develop less severe disease (51). We have previously shown that modulation of the Th1 response by an increased Th2 response reduces pathology associated with concurrent helminth infections (27). In the current study, the immune response of females to *H. pylori* infection was biased toward a greater Th1/Th2 ratio compared with males at both 6 and 12 mo. Higher Th1/Th2 ratios reflect a stronger inflammatory response to *H. pylori* infection. Furthermore, proinflammatory Th17 cells and regulatory T cells have been recently shown to modulate host responses to *H. pylori* (52, 53). *H. pylori*-specific Th17 immunity, mediated by IL-17 (54), increases inflammation unless it is suppressed by regulatory T cells, which are up-regulated by TGF-β and IL-10 (53). Higher levels of inflammation, epithelial defects, and atrophy were indeed observed in infected females at 6 MPI. At 12 MPI, the level of serum IgG2c was significantly elevated in infected females, reflective of increased proinflammatory cytokines in the gastric mucosa, and is consistent with the reduction in *H. pylori* colonization levels. The earlier onset of severe pathologic process caused by the Th1- and Th17-biased response to *H. pylori* was also associated with the increase in point mutations seen at 12 MPI.

In summary, we have shown that chronic *H. pylori* infection can cause premalignant gastric lesions and induce point mutations consistent with inflammatory processes. As our data are derived from analysis of nontranscribed DNA, it serves as an indicator of unbiased mutations reflecting genetic changes during the early stages of tumor initiation in inflamed tissues. At 12 mo, *H. pylori*-infected female C57BL/6 mice accumulate more inflammation-mediated point mutations compared with males as a result of a greater Th1-biased response to infection inducing earlier and more severe pathology. The sex-biased increase in premalignant gastric lesions and induction of mutations highlights the importance of taking into account sex-based effects in future studies of inflammation-driven disease.

Materials and Methods

Bacteria and Animals. *H. pylori* strain SS1 was grown on blood agar or *Brucella* broth with 5% FBS as described in *SI Materials and Methods*. Specific pathogen-free (including *Helicobacter* spp.) male and female C57BL/6 *gpt* delta mice (24) were infected by oral gavage with *H. pylori* SS1 or sham-dosed. At the indicated times, mice were euthanized, gastric tissue collected for histopathology and DNA and RNA extraction, and sera were collected for

cytokine and Ig analysis. Gastric lesions were scored for inflammation, epithelial defects, atrophy, hyperplasia, mucous metaplasia, hyalinosis, intestinal metaplasia, and dysplasia using previously published criteria (55). The GHAI is the sum of inflammation, epithelial defects, atrophy, hyperplasia, intestinal metaplasia, and dysplasia scores. A detailed description of the husbandry, treatment, and histopathology is provided in *SI Materials and Methods*.

DNA Isolation and in Vitro Packaging. Genomic DNA was extracted from gastric tissue using RecoverEase DNA Isolation Kit (Stratagene) following the manufacturer's recommendations. λ-EG10 phages were packaged in vitro from genomic DNA using the Transpack Packaging Extract (Stratagene) following the instructions.

***gpt* Assay and Sequencing Analysis.** The 6-TG selection assay was performed as previously described (24, 56). Briefly, phages rescued from murine genomic DNA were transfected into *E. coli* YG6020 expressing Cre recombinase. Infected cells were cultured on plates containing chloramphenicol (Cm) and 6-TG for 3 d until 6-TG–resistant colonies appeared. To confirm the 6-TG–resistant phenotype, colonies were restreaked on plates containing Cm and 6-TG. Confirmed 6-TG–resistant colonies were cultured, and a 739-bp DNA product containing the *gpt* gene was amplified by PCR. DNA sequencing of the *gpt* gene was performed by the Biopolymers Facility at Harvard Medical School (Boston, MA) with AMPure beads (Agencourt) and a 3730xL DNA Analyzer (Applied Biosystems). Sequences were aligned with the *E. coli gpt* gene (GenBank M13422.1) (57) using Geneious (Biomatters). Mutations were classified as transitions, transversions, deletions, insertions, or complex (multiple changes). Duplicate mutations at the same site within an individual tissue were excluded to account for clonal expansion of sibling mutations. More information on primers and methods is provided in *SI Materials and Methods*.

Spi⁻ Assay. The Spi⁻ assay was performed as described in *SI Materials and Methods*. Briefly, phages rescued from murine genomic DNA were transfected into *E. coli* strains with or without P2 lysogen. Infected cells were cultured overnight on λ-trypticase agar plates to allow plaque formation. The inactivation of *red* and *gam* genes was confirmed by respotting plaques on another *E. coli* strain with P2 lysogen (24).

mRNA Expression. RNA was extracted from gastric tissue and reverse-transcribed to cDNA. Quantitative real-time PCR was performed using TaqMan Gene Expression Assays (Applied Biosystems). TaqMan primers and analysis methods are described in *SI Materials and Methods*.

***H. pylori* Detection.** *H. pylori* levels in the gastric mucosa were quantified by real-time quantitative PCR assay of gastric DNA as described in *SI Materials and Methods*. A threshold of 15 copies of the *H. pylori* genome was set as the lower limit for a positive sample.

Serum IgG Isotype Measurement. Sera were analyzed for *H. pylori*-specific IgG2c and IgG1 by ELISA. Additional information on the measurements is provided in *SI Materials and Methods*.

Statistical Analysis. Two-way ANOVA followed by Bonferroni posttests were used to analyze GHAI and mRNA expression values. Student two-tailed *t* tests were used to analyze mutant and mutation frequency data and serum IgG isotypes. Poisson distribution analysis was used to determine hotspots at a 99% confidence level (58). For some analyses, age-matched controls of both sexes were grouped when no statistical differences were detected between sexes. Analyses were done with GraphPad Prism, version 4.0, or Microsoft Excel 2002. *P* < 0.05 was considered significant.

1. Fox JG, Wang TC (2007) Inflammation, atrophy, and gastric cancer. *J Clin Invest* 117: 60–69.
2. Suerbaum S, Michetti P (2002) Helicobacter pylori infection. *N Engl J Med* 347:1175–1186.
3. International Agency for Research on Cancer (1994) Schistosomes, liver flukes and Helicobacter pylori. IARC Working Group on the Evaluation of Carcinogenic Risks to Humans. Lyon, 7-14 June 1994. *IARC Monogr Eval Carcinog Risks Hum* 61:1–241.

4. Coussens LM, Werb Z (2002) Inflammation and cancer. *Nature* 420:860–867.
5. Obst B, Wagner S, Sewing KF, Beil W (2000) Helicobacter pylori causes DNA damage in gastric epithelial cells. *Carcinogenesis* 21:1111–1115.
6. Xu H, et al. (2004) Spermine oxidation induced by Helicobacter pylori results in apoptosis and DNA damage: Implications for gastric carcinogenesis. *Cancer Res* 64: 8521–8525.

MICROBIOLOGY

7. Davies GR, et al. (1994) Relationship between infective load of Helicobacter pylori and reactive oxygen metabolite production in antral mucosa. *Scand J Gastroenterol* 29: 419–424.
8. Davies GR, et al. (1994) Helicobacter pylori stimulates antral mucosal reactive oxygen metabolite production in vivo. *Gut* 35:179–185.
9. Mannick EE, et al. (1996) Inducible nitric oxide synthase, nitrotyrosine, and apoptosis in Helicobacter pylori gastritis: Effect of antibiotics and antioxidants. *Cancer Res* 56: 3238–3243.
10. Meira LB, et al. (2008) DNA damage induced by chronic inflammation contributes to colon carcinogenesis in mice. *J Clin Invest* 118:2516–2525.
11. Nair J, et al. (2006) Increased etheno-DNA adducts in affected tissues of patients suffering from Crohn's disease, ulcerative colitis, and chronic pancreatitis. *Antioxid Redox Signal* 8:1003–1010.
12. Zhuang JC, Lin C, Lin D, Wogan GN (1998) Mutagenesis associated with nitric oxide production in macrophages. *Proc Natl Acad Sci USA* 95:8286–8291.
13. Sato Y, et al. (2006) IL-10 deficiency leads to somatic mutations in a model of IBD. *Carcinogenesis* 27:1068–1073.
14. Bartsch H, Nair J (2004) Oxidative stress and lipid peroxidation-derived DNA-lesions in inflammation driven carcinogenesis. *Cancer Detect Prev* 28:385–391.
15. Nair U, Bartsch H, Nair J (2007) Lipid peroxidation-induced DNA damage in cancer-prone inflammatory diseases: a review of published adduct types and levels in humans. *Free Radic Biol Med* 43:1109–1120.
16. Kang JM, Iovine NM, Blaser MJ (2006) A paradigm for direct stress-induced mutation in prokaryotes. *FASEB J* 20:2476–2485.
17. Crabtree JE, Ferrero RL, Kusters JG (2002) The mouse colonizing Helicobacter pylori strain SS1 may lack a functional cag pathogenicity island. *Helicobacter* 7:139–140, author reply 140–141.
18. Lee A, Mitchell H, O'Rourke J (2002) The mouse colonizing Helicobacter pylori strain SS1 may lack a functional cag pathogenicity island: Response. *Helicobacter* 7:140–141.
19. Miyazawa M, et al. (2003) Suppressed apoptosis in the inflamed gastric mucosa of Helicobacter pylori-colonized iNOS-knockout mice. *Free Radic Biol Med* 34:1621–1630.
20. Jang J, et al. (2003) Malgun (clear) cell change in Helicobacter pylori gastritis reflects epithelial genomic damage and repair. *Am J Pathol* 162:1203–1211.
21. Lee H, et al. (2000) "Malgun" (clear) cell change of gastric epithelium in chronic Helicobacter pylori gastritis. *Pathol Res Pract* 196:541–551.
22. Touati E, et al. (2003) Chronic Helicobacter pylori infections induce gastric mutations in mice. *Gastroenterology* 124:1408–1419.
23. Jenks PJ, Jeremy AH, Robinson PA, Walker MM, Crabtree JE (2003) Long-term infection with Helicobacter felis and inactivation of the tumour suppressor gene p53 cumulatively enhance the gastric mutation frequency in Big Blue transgenic mice. *J Pathol* 201:596–602.
24. Nohmi T, et al. (1996) A new transgenic mouse mutagenesis test system using Spi- and 6-thioguanine selections. *Environ Mol Mutagen* 28:465–470.
25. Ihrig M, Whary MT, Dangler CA, Fox JG (2005) Gastric helicobacter infection induces a Th2 phenotype but does not elevate serum cholesterol in mice lacking inducible nitric oxide synthase. *Infect Immun* 73:1664–1670.
26. Lee CW, et al. (2008) Helicobacter pylori eradication prevents progression of gastric cancer in hypergastrinemic INS-GAS mice. *Cancer Res* 68:3540–3548.
27. Fox JG, et al. (2000) Concurrent enteric helminth infection modulates inflammation and gastric immune responses and reduces helicobacter-induced gastric atrophy. *Nat Med* 6:536–542.
28. De Bont R, van Larebeke N (2004) Endogenous DNA damage in humans: A review of quantitative data. *Mutagenesis* 19:169–185.
29. Burney S, Caulfield JL, Niles JC, Wishnok JS, Tannenbaum SR (1999) The chemistry of DNA damage from nitric oxide and peroxynitrite. *Mutat Res* 424:37–49.
30. Kadlubar FF, et al. (1998) Comparison of DNA adduct levels associated with oxidative stress in human pancreas. *Mutat Res* 405:125–133.
31. Pandya GA, Moriya M (1996) 1, N6-ethenodeoxyadenosine, a DNA adduct highly muta-genic in mammalian cells. *Biochemistry* 35:11487–11492.
32. Ambs S, et al. (1999) Relationship between p53 mutations and inducible nitric oxide synthase expression in human colorectal cancer. *J Natl Cancer Inst* 91:86–88.
33. Kim MY, Wogan GN (2006) Mutagenesis of the supF gene of pSP189 replicating in AD293 cells cocultivated with activated macrophages: roles of nitric oxide and reactive oxygen species. *Chem Res Toxicol* 19:1483–1491.
34. Dedon PC, Plastaras JP, Rouzer CA, Marnett LJ (1998) Indirect mutagenesis by oxidative DNA damage: formation of the pyrimidopurinone adduct of deoxyguanosine by base propenal. *Proc Natl Acad Sci USA* 95:11113–11116.
35. Jackson AL, Loeb LA (2001) The contribution of endogenous sources of DNA damage to the multiple mutations in cancer. *Mutat Res* 477:7–21.
36. Wood ML, Esteve A, Morningstar ML, Kuziemko GM, Essigmann JM (1992) Genetic effects of oxidative DNA damage: comparative mutagenesis of 7,8-dihydro-8-oxoguanine and 7,8-dihydro-8-oxoadenine in Escherichia coli. *Nucleic Acids Res* 20: 6023–6032.
37. Pang B, et al. (2007) Lipid peroxidation dominates the chemistry of DNA adduct formation in a mouse model of inflammation. *Carcinogenesis* 28:1807–1813.
38. Masumura K, et al. (2003) Low dose genotoxicity of 2-amino-3,8-dimethylimidazo[4,5-f]quinoxaline (MeIQx) in gpt delta transgenic mice. *Mutat Res* 541:91–102.
39. Masumura K, et al. (2000) Characterization of mutations induced by 2-amino-1-methyl-6-phenylimidazo[4,5-b]pyridine in the colon of gpt delta transgenic mouse: novel G:C deletions beside runs of identical bases. *Carcinogenesis* 21:2049–2056.
40. Balkwill F, Coussens LM (2004) Cancer: An inflammatory link. *Nature* 431:405–406.
41. Clevers H (2004) At the crossroads of inflammation and cancer. *Cell* 118:671–674.
42. Court M, Robinson PA, Dixon MF, Jeremy AH, Crabtree JE (2003) The effect of gender on Helicobacter felis-mediated gastritis, epithelial cell proliferation, and apoptosis in the mouse model. *J Pathol* 201:303–311.
43. Fox JG, et al. (2002) Germ-line p53-targeted disruption inhibits helicobacter-induced premalignant lesions and invasive gastric carcinoma through down-regulation of Th1 proinflammatory responses. *Cancer Res* 62:696–702.
44. Lee A, Fox JG, Otto G, Murphy J (1990) A small animal model of human Helicobacter pylori active chronic gastritis. *Gastroenterology* 99:1315–1323.
45. Taylor NS, et al. (1995) Long-term colonization with single and multiple strains of Helicobacter pylori assessed by DNA fingerprinting. *J Clin Microbiol* 33:918–923.
46. Lemke LB, et al. (2009) Concurrent Helicobacter bilis infection in C57BL/6 mice attenuates proinflammatory H. pylori-induced gastric pathology. *Infect Immun* 77: 2147–2158.
47. Crabtree JE, et al. (2004) Gastric mucosal cytokine and epithelial cell responses to Helicobacter pylori infection in Mongolian gerbils. *J Pathol* 202:197–207.
48. Fox JG, et al. (2003) Host and microbial constituents influence Helicobacter pylori-induced cancer in a murine model of hypergastrinemia. *Gastroenterology* 124:1879–1890.
49. Bamford KB, et al. (1998) Lymphocytes in the human gastric mucosa during Helicobacter pylori have a T helper cell 1 phenotype. *Gastroenterology* 114:482–492.
50. Mohammadi M, Czinn S, Redline R, Nedrud J (1996) Helicobacter-specific cell-mediated immune responses display a predominant Th1 phenotype and promote a delayed-type hypersensitivity response in the stomachs of mice. *J Immunol* 156: 4729–4738.
51. Sakagami T, et al. (1996) Atrophic gastric changes in both Helicobacter felis and Helicobacter pylori infected mice are host dependent and separate from antral gastritis. *Gut* 39:639–648.
52. Lee CW, et al. (2007) Wild-type and interleukin-10-deficient regulatory T cells reduce effector T-cell-mediated gastroduodenitis in Rag2-/- mice, but only wild-type regulatory T cells suppress Helicobacter pylori gastritis. *Infect Immun* 75:2699–2707.
53. Kao JY, et al. (2010) Helicobacter pylori immune escape is mediated by dendritic cell-induced Treg skewing and Th17 suppression in mice. *Gastroenterology* 138:1046–1054.
54. Xu S, Cao X (2010) Interleukin-17 and its expanding biological functions. *Cell Mol Immunol* 7:164–174.
55. Rogers AB, et al. (2005) Helicobacter pylori but not high salt induces gastric intraepithelial neoplasia in B6129 mice. *Cancer Res* 65:10709–10715.
56. Masumura K, et al. (1999) Spectra of gpt mutations in ethylnitrosourea-treated and untreated transgenic mice. *Environ Mol Mutagen* 34:1–8.
57. Nüesch J, Schümperli D (1984) Structural and functional organization of the gpt gene region of Escherichia coli. *Gene* 32:243–249.
58. Kim MY, Dong M, Dedon PC, Wogan GN (2005) Effects of peroxynitrite dose and dose rate on DNA damage and mutation in the supF shuttle vector. *Chem Res Toxicol* 18: 76–86.

Research Article

Antigenotoxic Effects of *p53* on Spontaneous and Ultraviolet Light B–Induced Deletions in the Epidermis of *gpt* Delta Transgenic Mice

Kenichi Masumura,[1] Yasuteru Sakamoto,[1] Megumi Ikeda,[1,2] Yasuo Asami,[1]
Tetsuya Tsukamoto,[3] Hironobu Ikehata,[4] Yuichi Kuroiwa,[5]
Takashi Umemura,[5] Akiyoshi Nishikawa,[5] Masae Tatematsu,[3]
Tetsuya Ono,[4] and Takehiko Nohmi[1]*

[1] *Division of Genetics and Mutagenesis, National Institute of Health Sciences, Tokyo, Japan*
[2] *School of Nutrition and Dietetics, Kanagawa University of Human Services, Kanagawa, Japan*
[3] *Division of Oncological Pathology, Aichi Cancer Center Research Institute, Nagoya, Japan*
[4] *Department of Cell Biology, Tohoku University Graduate School of Medicine, Sendai, Japan*
[5] *Division of Pathology, National Institute of Health Sciences, Tokyo, Japan*

Tumor development in the skin may be a multistep process where multiple genetic alterations occur successively. The *p53* gene is involved in genome stability and thus is referred to as "the guardian of the genome." To better understand the antigenotoxic effects of *p53* in ultraviolet light B (UVB)-induced mutagenesis, mutations were measured in the epidermis of UVB-irradiated *p53*+/+ and *p53*−/− *gpt* delta mice. In the mouse model, point mutations and deletions are separately identified by the *gpt* and Spi− assays, respectively. The mice were exposed to UVB at single doses of 0.5, 1.0, or 2.0 kJ/m². The mutant frequencies (MFs) were determined 4 weeks after the irradiation. All doses of UVB irradiation enhanced *gpt* MFs by about 10 times than that of unirradiated mice. There were no significant differences in *gpt* MFs and the mutation spectra between *p53*+/+ and *p53*−/− mice. The predominant mutations induced by UVB irradiation were G:C to A:T transitions at dipyrimidines. In contrast, in unirradiated *p53*−/− mice, the frequencies of Spi− large deletions of more than 1 kb and complex-type deletions with rearrangements were significantly higher than those of the Spi− large deletions in *p53*+/+ counterparts. The specific Spi− mutation frequency of more than 1 kb deletions and complex types increased in a dose-dependent manner in the *p53*+/+ mice. However, no increase of such large deletions was observed in irradiated *p53*−/− mice. These results suggest that the antigenotoxic effects of *p53* may be specific to deletions and complex-type mutations induced by double-strand breaks in DNA. Environ. Mol. Mutagen. 52:244–252, 2011. © 2010 Wiley-Liss, Inc.

Key words: Spi; deletion mutations; dipyrimidines; mutation frequency

INTRODUCTION

The *p53* gene is involved in various aspects of genome stability and thus is referred to as "the guardian of the genome." Several strains of transgenic mice were developed in which a major part of *p53* was deleted [Donehower et al., 1992; Tsukada et al., 1993; Jacks et al., 1994; Purdie et al., 1994], and each of these knockout strains has a propensity to develop thymic lymphoma at an early stage. However, no significant difference in spontaneous *lacI* mutant frequencies (MFs) has been reported between *p53*+/+ and *p53*−/− mice [Nishino et al., 1995; Buettner et al., 1996]. In addition, *lacI* MFs induced after exposure to 4-nitroquinoline 1-oxide (4-NQO) are not significantly different between *p53*+/+ and *p53*−/− mice [Sands et al., 1995]. Because the *lacI* transgene preferentially detects point mutations [Nishino et al., 1995], it was suggested that *p53* deficiency did not affect accumulation of

Environmental and Molecular Mutagenesis. DOI 10.1002/em

Effects of *p53* on Deletions in the Murine Epidermis   245

point mutations in vivo. However, it remains uncertain, whether *p53* deficiency affects other types of mutations or chromosome aberrations. In fact, a study with the endogenous *aprt* gene, which detects loss of heterozygosity (LOH) induced by chromosome aberrations and point mutations, showed that frequencies of chromosome aberrations were significantly increased in $p53^{-/-}$ mice compared with $p53^{+/+}$ [Shao et al., 2000]. Another study, using the endogenous p^{un} reversion mutation assay, suggested that *p53* was involved in X-ray-induced intrachromosomal recombination [Aubrecht et al., 1999]. Loss of *p53* function was associated with an increase in the frequency of LOH within the *tk* gene in TK6 human cells in vitro [Morris, 2002]. These studies suggest that the effect of *p53* loss may be influential in deletions and/ or rearrangement-type mutations induced by DNA double-strand breaks (DSB).

To further investigate the effects of *p53* on point mutations and deletions in vivo, we analyzed mutations in the epidermis of $p53^{+/+}$ and $p53^{-/-}$ gpt delta mice exposed to ultraviolet light B (UVB) irradiation. In this mouse model, point mutations and deletions are separately identified by the *gpt* and Spi⁻ assays [Nohmi et al., 1996, 2000; Nohmi, 2007]. UVB is responsible for most carcinogenic effects of sun exposure. The sunlight-induced mutation spectrum is highly UV-specific, quite similar to that induced by UVB [Ikehata et al., 2004]. UVB irradiation induces not only point mutations, such as G:C to A:T transitions, but also deletions of more than 1 kb in the epidermis of *gpt* delta mice [Horiguchi et al., 1999, 2001]. In this study, we demonstrated that Spi⁻ MFs in unirradiated $p53^{-/-}$ mice were significantly higher than that in $p53^{+/+}$ counterparts. In the $p53^{-/-}$ background, large deletions greater than 1 kb in size and complex-type rearrangements were much more frequently observed, compared with the $p53^{+/+}$ counterparts. Interestingly, the specific Spi⁻ mutation frequency of the large deletions and complex types increased in a dose-dependent manner in the $p53^{+/+}$ mice. However, no increase in frequencies of such large deletions was observed in irradiated $p53^{-/-}$ mice. There were no significant differences in the *gpt* MF and spectra between $p53^{+/+}$ and $p53^{-/-}$ mice regardless of the presence or the absence of UVB irradiation. The results suggest that *p53* affects the induction of deletions and rearrangements but not the induction or accumulation of point mutations in vivo.

MATERIALS AND METHODS

UVB Irradiation of $p53^{+/+}$ and $p53^{-/-}$ gpt Delta Mice

Homozygous *gpt* delta transgenic mice of C57BL/6J genetic background [Nohmi et al., 2000] were mated with $p53^{+/-}$ mice of C57BL/6J background [Tsukada et al., 1993], and $p53^{+/-}$ gpt delta mice were obtained. We obtained $p53^{+/+}$ and $p53^{-/-}$ gpt delta mice by intercrossing $p53^{+/-}$ gpt delta mice. Genotypes of the *p53* and *gpt* genes were examined by polymerase chain reaction (PCR) as described in the study of Tsukada et al. (1993), Nohmi et al. (1996). In this study, male $p53^{+/+}$ and

$p53^{-/-}$ gpt delta mice (6–10 weeks old) were used. The experimental protocol described in the following sections was approved by the Animal Care and Utilization Committee of the National Institute of Health Sciences. For UVB irradiation of the skin, the hair on the back was removed using a clipper and hair removing cream under anesthesia. Four days later, the mice were exposed to UVB at a single dose of 0.5, 1.0, or 2.0 kJ/m² (0.3 kJ/m²/min) under anesthesia. The UV source was a model UVM-57 (UVP, Upland, CA). Dose rate was measured by a UVX-31 Radiometer (UVP, Upland, CA). Irradiation was performed in a CHROMATO-VUE® CABINET model CC-10 (UVP, Upland, CA). Four mice were used in each group. They were sacrificed 4 weeks later and the back skin was collected and stored at -80°C. The epidermis was separated from the skin using thermolysin treatment and genomic DNA was extracted by the phenol/chloroform/isoamyl alcohol method [Ikehata et al., 2001]. Lambda EG10 phages were rescued from the genomic DNA by in vitro packaging reactions using Transpack® packaging extract (Stratagene, La Jolla, CA) and used for the following mutation assays.

Mutation Assay and Sequencing Analysis

The *gpt* mutation assay was performed as described previously [Nohmi et al., 2000]. The rescued phages were used to infect *E. coli* strain YG6020 expressing Cre recombinase to convert the transgene to plasmid. Infected cells were mixed with molten soft agar and poured onto agar plates containing chloramphenicol (Cm) and 6-thioguanine (6-TG). The plates were incubated for 3 days at 37°C to select for colonies harboring the plasmid carrying the mutated *gpt* gene. Infected cells were also poured on plates containing Cm without 6-TG to determine the number of rescued plasmids. The *gpt* MF was calculated as described previously [Nohmi et al., 2000]. The selected 6-TG–resistant mutants were cultured and collected. A 739-bp DNA fragment containing the mutated *gpt* gene was amplified by PCR [Nohmi et al., 2000]. DNA sequencing of the *gpt* gene was performed with BigDye® Terminator Cycle Sequencing Ready Reaction (Applied Biosystems, Foster City, CA) on a ABI PRISM® 3100 Genetic Analyzer (Applied Biosystems, Foster City, CA). The sequencing primer was the gptA2 primer (5'-TCTCGCGCAACCTATTTTCCC-3'). Clonally corrected mutation spectra were estimated, that is, counting the same mutation from the same animal as one mutation.

The Spi⁻ mutation assay was performed as described previously [Nohmi et al., 2000] with some modifications. We added 10 mM MgSO₄ to both agar plates and soft agar to improve the detection efficiency of Spi⁻ plaques, as described previously [Shibata et al., 2003]. The rescued phages from the genomic DNA of $p53^{+/+}$ and $p53^{-/-}$ gpt delta mice were used to infect *E. coli* XL1-Blue MRA (P2). Infected cells were mixed with molten soft agar, poured onto lambda-trypticase agar plates, and incubated at 37°C. The plaques detected on the plates (Spi⁻ candidates) were suspended in 50 μl of SM buffer. The suspension was spotted on two types of plates, spread with either XL1-Blue MRA (P2) or the WL95 (P2) strain. The plates were incubated overnight at 37°C. The number of mutants that made clear spots on both strains was counted as confirmed Spi⁻ mutants. The Spi⁻ MF was calculated as described previously [Nohmi et al., 2000]. The MFs were corrected for potential clonal expansion. The lysates of the Spi⁻ mutants were obtained by infection of *E. coli* LE392 with the recovered Spi⁻ mutants. The lambda DNA was extracted from the lysates with the Quantum Prep® AquaPure™ Genomic DNA Isolation Kit (BIO-RAD, Hercules, CA). The lysate and extracted DNA were used as templates for PCR analysis to determine the deleted regions. The DNA fragments containing the deletions which were amplified by PCR using primers 001–002 (5 kb in length), 005–012 (14 kb), or 005–006 (21 kb), followed by sequencing analysis of the PCR products. The PCR primers were:

- primer 001 (5'-CTCTCCTTTGATGCGAATGCCAGC-3'),
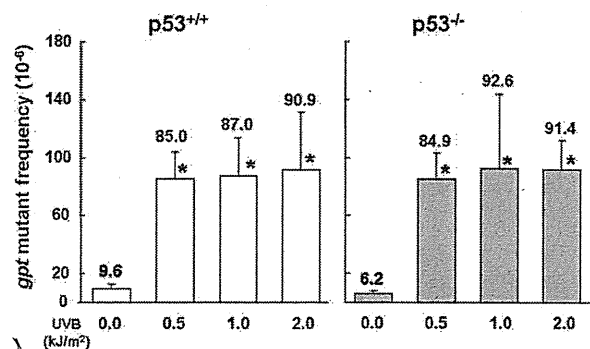- primer 002 (5'-GGAGTAATTATGCGGAACAGAATCATGC-3'),

Fig. 1. *gpt* MFs in the epidermis of UVB-irradiated $p53^{+/+}$ and $p53^{-/-}$ *gpt* delta mice. * Denotes $P < 0.05$ ($n = 4$) in Dunnett test (for $p53^{+/+}$) or Kruskal–Wallis test (for $p53^{-/-}$) comparing the MFs of UVB-irradiated versus the corresponding unirradiated mice. Vertical bars show the standard deviations with mice as the unit of comparison.

- primer 005 (5'-CGTGGTCTGAGTGTGTTACAGAGG-3'),
- primer 006 (5'-GTTATGCGTTGTTCCATACAACCTCC-3'), and
- primer 012 (5'-CGGTCGAGGGACCTAATAACTTCG-3').

Sequence changes within and outside of the *gam/redBA* genes were identified by DNA sequencing analysis. The appropriate primers for DNA sequencing were selected based on the results of PCR analysis. The entire sequence of lambda EG10 is available at http://dgm2alpha.nihs.go.jp.

Statistical Analysis

All data are expressed as mean ± SD. Statistical analyses were performed by analysis of variance followed by parametric (Dunnett) or nonparametric (Kruskal–Wallis) test to compare between two groups. Cochran–Armitage trend test was applied for significance of dose-dependent increase as noted in a detailed review of transgenic rodent mutation assays [Lambert et al., 2005]. A comparison of mutational spectra was performed using Adams–Skopek test [Adams and Skopek, 1987; Cariello et al., 1994]. A P value less than 0.05 denoted a statistically significant difference.

RESULTS

Increased *gpt* MFs in the Epidermis of UVB-Irradiated $p53^{+/+}$ and $p53^{-/-}$ Mice

The *gpt* MFs in the epidermis of $p53^{+/+}$ and $p53^{-/-}$ *gpt* delta mice were significantly increased by UVB irradiation at 0.5, 1.0, or 2.0 kJ/m^2 compared with unirradiated mice (Fig. 1). In $p53^{+/+}$ mice, *gpt* MFs of the irradiated groups were 85.0–90.9 × 10^{-6}, which were similar to those of the irradiated groups of the $p53^{-/-}$ mice (84.9–92.6 × 10^{-6}). These values were 9–15 times higher than those of unirradiated mice (9.6 × 10^{-6} and 6.2 × 10^{-6}, respectively, for $p53^{+/+}$ and $p53^{-/-}$ mice). The *gpt* MFs in the unirradiated groups were not significantly different between $p53^{+/+}$ and $p53^{-/-}$ mice. There were no dose-dependent increases in *gpt* MFs regardless of the

p53 status. This may suggest that *gpt* MFs in the epidermis were saturated at UVB doses greater than 0.5 kJ/m^2.

Induction of G:C to A:T Transitions at Dipyrimidines in the Epidermis of UVB-Irradiated $p53^{+/+}$ and $p53^{-/-}$ Mice

To investigate the type of mutations induced by UVB irradiation, we determined the *gpt* mutation spectra in the epidermis of $p53^{+/+}$ and $p53^{-/-}$ *gpt* delta mice (Tables I and II). In UVB-irradiated $p53^{+/+}$ mice, G:C to A:T transitions were the predominant mutations, i.e., 78% (28/36), 76% (22/29), and 74% (28/38) at 0.5, 1.0, and 2.0 kJ/m^2, respectively. Most of the G:C to A:T transitions were observed on the 3' side of the dipyrimidines that were 5'-C**C**-3' and 5'-T**C**-3', that is, 93% (26/28), 95% (21/22), and 86% (24/28) of G:C to A:T transitions for 0.5, 1.0, and 2.0 kJ/m^2, respectively. No significant differences in the *gpt* mutation spectra were observed between UVB-irradiated groups. In UVB-irradiated $p53^{-/-}$ mice, G:C to A:T transitions were 65% (22/34), 81% (29/36), and 69% (20/28) of mutations for 0.5, 1.0, and 2.0 kJ/m^2, respectively. The G:C to A:T transitions observed on the 3' side of the dipyrimidines, 5'-C**C**-3' and 5'-T**C**-3', were 91% (20/22), 83% (24/29), and 95% (19/20) of G:C to A:T transitions for 0.5, 1.0, and 2.0 kJ/m^2, respectively. The tandem base substitution, 5'-C**C**-3' to 5'-**TT**-3', was observed in $p53^{+/+}$ and $p53^{-/-}$ mice. The characteristics of the *gpt* mutation spectra were similar between irradiated $p53^{+/+}$ and $p53^{-/-}$ mice ($P = 0.91$, Adams–Skopek test). In untreated mice, base substitutions such as G:C to A:T, G:C to T:A, and A:T to T:A were observed in both $p53^{+/+}$ (86%, 32/37) and $p53^{-/-}$ (89%, 16/18) mice.

High-Spontaneous Spi$^-$ MFs in $p53^{-/-}$ Mice

To investigate the induction of deletions, Spi$^-$ MFs in the epidermis of $p53^{+/+}$ and $p53^{-/-}$ *gpt* delta mice were determined. In $p53^{+/+}$ mice, Spi$^-$ MFs were significantly increased by UVB irradiation at 1.0 or 2.0 kJ/m^2 compared with those of unirradiated mice (Table III). The Spi$^-$ MFs were increased four times for the 1.0 and 2.0 kJ/m^2 doses compared with the control level. In $p53^{-/-}$ mice, the Spi$^-$ MF of unirradiated mice was 4.91 × 10^{-6}, which was 2.5 times higher than that of $p53^{+/+}$ mice (1.96 × 10^{-6}). In the UVB-irradiated groups, Spi$^-$ MFs were 1.2- to 1.7-fold higher but not significantly different from those of the unirradiated mice.

Characteristics of Spi$^-$ Large Deletions in $p53^{+/+}$ and $p53^{-/-}$ Mice

To characterize the UVB-induced deletion mutations in more detail, the Spi$^-$ mutants rescued from the epidermis were subjected to PCR analysis. The Spi$^-$ mutants that had the deletions with the sizes more than 1 kb were selected and analyzed by DNA sequencing. The specific

Environmental and Molecular Mutagenesis. DOI 10.1002/em

Effects of *p53* on Deletions in the Murine Epidermis 247

TABLE I. *gpt* Mutation Spectra in the Epidermis of UVB-Irradiated *p53*^{+/+} *gpt* Delta Mice

	0 kJ/m²		0.5 kJ/m²		1.0 kJ/m²		2.0 kJ/m²	
	No.	MF[a] ($\times 10^{-6}$)	No.	MF ($\times 10^{-6}$)	No.	MF ($\times 10^{-6}$)	No.	MF ($\times 10^{-6}$)
Base substitution								
Transition								
G:C → A:T	24 (6)	6.2	28 (3)	66.1	22 (2)	66.0	28 (3)	66.9
A:T → G:C	1	0.3	0	0.0	2	6.0	1	2.4
Transversion								
G:C → T:A	6	1.6	2	4.7	0	0.0	2	4.8
G:C → C:G	1	0.3	1	2.4	0	0.0	0	0.0
A:T → T:A	2	0.5	3	7.1	3	9.0	2	4.8
A:T → C:G	0	0.0	0	0.0	1	3.0	1	2.4
Tandem base substitution	0	0.0	1	2.4	1	3.0	3	7.2
Deletion	1	0.3	0	0.0	0	0.0	1	2.4
−1 bp	0		0		0		1	
>2 bp	1		0		0		0	
Insertion	0	0.5	0	0.0	0	0.0	0	0.0
Others[b]	0	0.0	1	2.4	0	0.0	0	0.0
Total no.	37	9.6	36	85.0	29	87.0	38	90.9

[a]MFs are calculated by dividing total MF by the ratio of each type of mutations.
[b]Others: TAA to AAG.
( )=CpG sites.

TABLE II. *gpt* Mutation Spectra in the Epidermis of UVB-Irradiated *p53*^{−/−} *gpt* Delta Mice

	0 kJ/m²		0.5 kJ/m²		1.0 kJ/m²		2.0 kJ/m²	
	No.	MF[a] ($\times 10^{-6}$)	No.	MF ($\times 10^{-6}$)	No.	MF ($\times 10^{-6}$)	No.	MF ($\times 10^{-6}$)
Base substitution								
Transition								
G:C → A:T	13 (1)	4.5	22 (2)	54.9	29 (4)	74.6	20	63.1
A:T → G:C	0	0.0	4	10.0	1	2.6	0	0.0
Transversion								
G:C → T:A	1	0.3	0	0.0	0	0.0	4	12.6
G:C → C:G	0	0.0	0	0.0	1	2.6	0	0.0
A:T → T:A	2	0.7	2	5.0	1	2.6	2	6.3
A:T → C:G	0	0.0	2	5.0	1	2.6	0	0.0
Tandem base substitution	2	0.7	3	7.5	1	2.6	0	0.0
Deletion	0	0.0	0	0.0	1	2.6	1	3.2
−1 bp	0		0		1		1	
>2 bp	0		0		0		0	
Insertion	0	0.0	1	2.5	0	0.0	1	3.2
Others[b]	0	0.0	0	0.0	1	2.6	1	3.2
Total no.	18	6.2	34	84.9	36	92.6	28	91.4

[a]MFs are calculated by dividing total MF by the ratio of each type of mutations.
[b]Others = TCA to TT, CCT to CA.
( )=CpG sites.

Spi⁻ mutation frequencies of large deletions (greater than 1 kb) and complex (deletion with rearrangement) types are shown in Figure 2. In this study, "complex types" were defined as deletion mutants whose junctions were unable to be identified by PCR and sequencing analyses because of the complex rearrangements. In the *p53*^{+/+} mice, the specific Spi⁻ mutation frequency increased in a dose-dependent manner ($P = 0.01$ in Cochran–Armitage trend test), and was about five times higher at 2.0 kJ/m² (0.93×10^{-6}) than that of the unirradiated mice (0.17×10^{-6}). On the other hand, the specific Spi⁻ mutation fre-

quency of large deletions in unirradiated *p53*^{−/−} mice was significantly higher than that of unirradiated *p53*^{+/+} mice (1.58×10^{-6} compared with 0.17×10^{-6}, $P = 0.04$ in Dunnett test). No significant increase in the specific Spi⁻ mutation frequency of large deletions was observed in three irradiated groups of *p53*^{−/−} mice. We identified the size and junctions of 39 Spi⁻ deletions and summarized the nature of the large deletions (greater than 1 kb) recovered from both *p53*^{+/+} and *p53*^{−/−} mice (Fig. 3). The largest deletion size was −7,094 bp. The identical mutation was recovered multiple times from the

TABLE III. Spi⁻ Mutant Frequency in the Epidermis of UVB-Irradiated *gpt* Delta Mice

UVB (kJ/m²)	Animal ID	Total population	No. of mutants	MF ($\times 10^{-6}$)	Average	SD
p53⁺/⁺						
0.0	101	1,569,000	5	3.19	1.96	0.89
	102	3,411,000	4	1.17		
	103	1,506,000	3	1.99		
	104	1,361,500	2	1.47		
0.5	201	1,389,000	5	3.60	4.14	1.79
	202	1,629,000	11	6.75		
	203	2,250,000	6	2.67		
	204	1,131,000	4	3.54		
1.0	301	1,907,000	6	3.15	7.31*	3.98
	302	1,421,500	18	12.66		
	303	1,158,000	7	6.04		
	304	1,083,000	8	7.39		
2.0	401	1,038,000	9	8.67	8.24**	0.45
	402	1,800,000	14	7.78		
	403	1,569,000	13	8.29		
	404			ND		
p53⁻/⁻						
0.0	501	1,735,000	10	5.76	4.91	2.74
	502	714,000	6	8.40		
	503	1,608,000	4	2.49		
	504	1,002,000	3	2.99		
0.5	601	783,000	9	11.49	8.30	2.46
	602	1,005,000	8	7.96		
	603	1,995,000	11	5.51		
	604	1,461,000	12	8.21		
1.0	701	1,344,000	12	8.93	6.04	2.16
	702	1,551,000	9	5.80		
	703	2,442,000	9	3.69		
	704	1,743,000	10	5.74		
2.0	801	1,275,000	15	11.76	8.06	3.47
	803	1,209,000	6	4.96		
	804	1,365,000	14	10.26		
	805	3,048,000	16	5.25		

*Denotes $P < 0.05$ in Dunnett test comparing the MFs of UVB-irradiated versus the corresponding unirradiated mice.
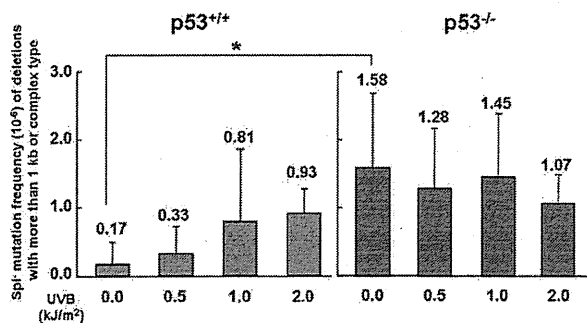**Denotes $P < 0.01$.

Fig. 2. Specific Spi⁻ mutation frequencies of large deletions (greater than 1 kb) and complex-type deletions in the epidermis of UVB-irradiated *p53⁺/⁺* and *p53⁻/⁻ gpt* delta mice. * Denotes $P < 0.05$ ($n = 4$) for the MFs of *p53⁻/⁻* mice versus the corresponding *p53⁺/⁺* mice (Dunnett test). Vertical bars show the standard deviations with mice as the unit of comparison.

same group: -3,979 bp deletions were recovered from three of four mice for each group (0.5, 1.0, or 2.0 kJ/m²) of UVB-irradiated *p53⁻/⁻* mice. The identical complex type was recovered from four mice with *p53⁻/⁻* background irradiated with 1.0 kJ/m² UVB.

DISCUSSION

The tumor suppressor gene *p53* plays important roles in the maintenance of genome integrity. To characterize the antimutagenic potential of *p53* in skin carcinogenesis, where *p53* is frequently inactivated by sunlight [Brash et al., 1991], we compared the frequencies and spectra of *gpt* and Spi⁻ mutations in *p53⁺/⁺* and *p53⁻/⁻ gpt* delta mice. The *gpt* MFs in the epidermis of *p53⁺/⁺* and *p53⁻/⁻* mice were significantly increased by UVB irradiation at 0.5, 1.0, or 2.0 kJ/m² compared with those of unirradiated mice (Fig. 1). However, there were no substantial differences in *gpt* MF between *p53⁺/⁺* and *p53⁻/⁻* mice. The *gpt* mutation spectra were also similar between *p53⁺/⁺* and *p53⁻/⁻* mice (Tables

Environmental and Molecular Mutagenesis. DOI 10.1002/em

Effects of p53 on Deletions in the Murine Epidermis   249

λ EG10

UVB (kJ/m²)   redBA gam   Deletion size   Sequence at junction

p53⁺/⁺

0.0   -3979 bp   CGGACTTCGTTGCTTTCCAG TTTA TTTTTCAATAAATACA

0.5   Complex   GTCGTAGCAGTCGTTGATGT GCGGCGAAGTGGGTTCTGCG
       Complex   Not identified

1.0   -3537 bp   CTGAATCAATATCAACCTGG AAACCTTCCGGGGTCTTTTC
       -3979 bp   CGGACTTCGTTGCTTTCCAG TTTA TTTTTCAATAAATACA
       Complex   AAATGCCGTCTGG TTGCCCCGTATTCAGTGT TGCTCATAGTGTG
       Complex   Not identified

2.0   -2975 bp   TCGAAACCACCGAGCCGGAA CT GTTCCGCATAATTACTCC
       -6147 bp   TCCAGGTCACCAGTGCAGTG C ACTAACACCCAGTCAGCCT
       -7094 bp   GATATTATCGTGAGGATGCG TCA GCGCCTGTTCAAGACGT
       Complex   Not identified

p53⁻/⁻

0.0   -1768 bp   GACAGCTCTCACATCGATCC C ACATTGGCAGCTAATCCGG
       -3633 bp   CCAGTTCTGCCTCTTTCTCT CACTGAGCGCATCATCAAAC
       -3979 bp   CGGACTTCGTTGCTTTCCAG TTTA TTTTTCAATAAATACA
       -4835 +6 bp   CATAAACCATCGGGAGAGCA CTCCCA AATCACTCCCAAAA
       -5513 bp   ATAACTCAATGTTGGCCTGT GTTCTGGCAAAACCAATGGT
       -6107 bp   TATTATAAAACAGTGAGAGG T CGATGCATAGCGATTCAAA
       Complex   AATATCCTGCATTCCCGAAC C GCGGGTTTTCGCTATTTAT...?
       Complex   GTTCATCCAGCAGTTCCAGC TAGATGAAGAGCAAGCGCAT...?

0.5   -1077 bp   ATCAAACGCACGGGTAATGG ATTTTTTGCAGGGGGGCATT
       -2981 bp   TCCAGTTTAGCAATACGCTT A ATGTAATAAGCGTTCATGG
       -3979 bp *   CGGACTTCGTTGCTTTCCAG TTTA TTTTTCAATAAATACA

1.0   -3979 bp *   CGGACTTCGTTGCTTTCCAG TTTA TTTTTCAATAAATACA
       -4255 bp   AAGGCCGTTGCCGTCACTGC GCGGGAATCATGCGGGTGAG
       Complex **   Not identified

2.0   -1295 bp   TTCGCGGCGGCATTCATCCA TCCTGAACGAAAACCCCCCG
       -3979 bp *   CGGACTTCGTTGCTTTCCAG TTTA TTTTTCAATAAATACA
       -4775 bp   GATGGTGTTACCAATTCATG GA TTAAAAAATCTGTCAGAT
       -5753 +93 bp   ATATGAAGCCCGCTGC ATGTGT...CCTGCA TCAGCGACTGTTCGAT
       -6107 bp   TATTATAAAACAGTGAGAGG T CGATGCATAGCGATTCAAA

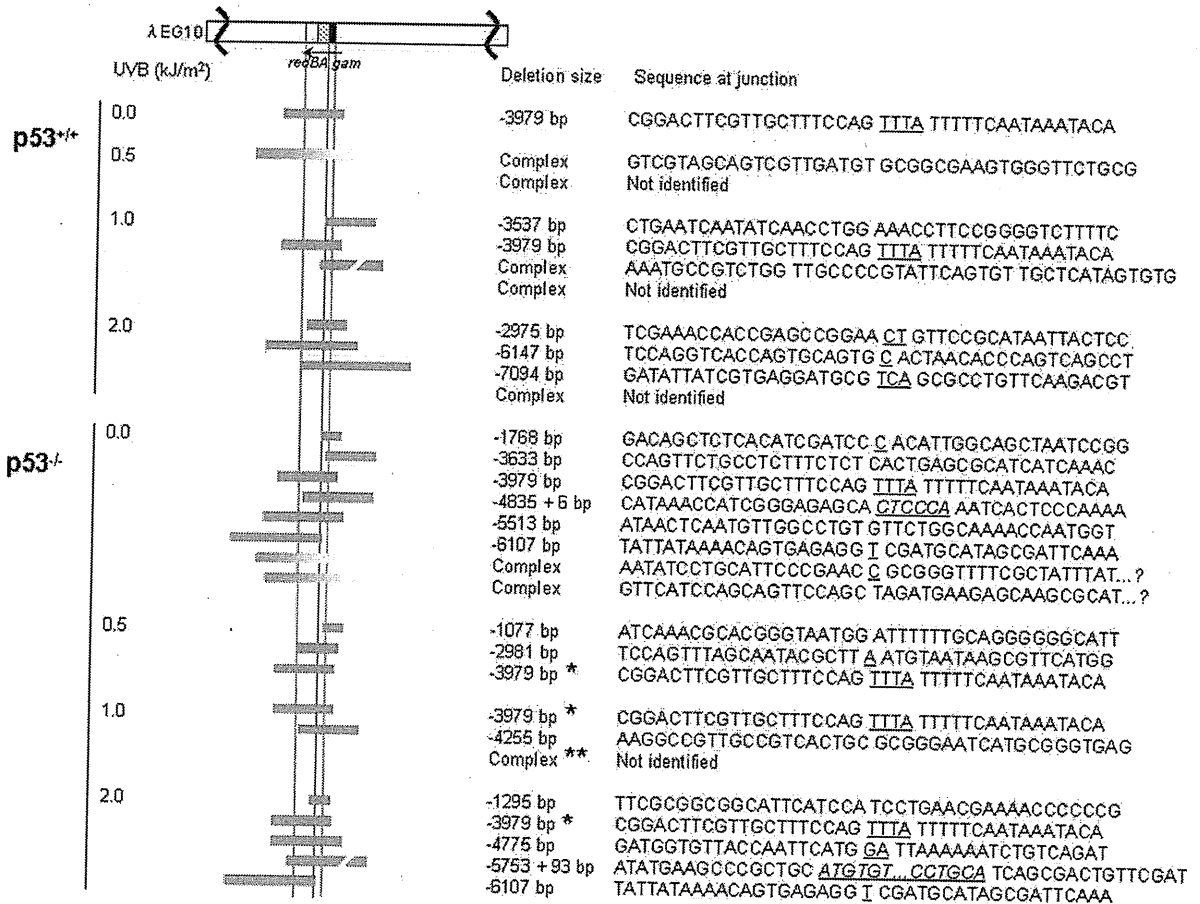**Fig. 3.** Molecular nature of large deletions recovered from the epidermis of UVB-irradiated p53⁺/⁺ and p53⁻/⁻ gpt delta mice. A partial genetic map of the lambda EG10 transgene including the gam and redBA target region of Spi⁻ selection is shown in the upper part. Horizontal gray bars represent the deleted regions of mutants. Junctions are indicated as spaces between left and right sequences. Short homologous sequences in the junctions of the mutants are underlined. Underlined, italicized sequences are inserted sequences. *The identical independent mutant was recovered multiple times from the same group: the -3979 bp deletion was recovered from three of four mice for each group (0.5, 1.0, or 2.0 kJ/m²) of UVB-irradiated p53⁻/⁻ mice. The complex types were recovered from four p53⁻/⁻ mice irradiated with 1.0 kJ/m² UVB.

I and II). The most frequent point mutations in the epidermis of UVB-irradiated mice were G:C to A:T transitions induced at dipyrimidine sites, such as 5'-TC-3' and 5'-CC-3', which were 86–95% and 83–95% of total G:C to A:T transitions in UVB-irradiated p53⁺/⁺ and p53⁻/⁻ mice, respectively. From studies on UVB-irradiated *E. coli*, mammalian cells, and the p53 gene in nonmelanoma skin cancer, it is known that UVB irradiation generates cyclobutane pyrimidine dimers (CPD) and pyrimidime(6-4)pyrimidome photoproducts (6-4PP) at dipyrimidine sites and induces G:C to A:T base substitutions [Miller, 1985; Hauser et al., 1986; Hsia et al., 1989; Brash et al., 1991; Ziegler et al., 1993; Daya-Grosjean et al., 1995]. The spectra of UVB-induced mutations in the epidermis of Muta™ mice were reported to be dominated by G:C to A:T transitions at dipyrimidine sites in the lacZ transgene [Ikehata et al., 2003]. The results in this study and previous reports suggest that UVB-induced photo-

products cause characteristic mutations at similar efficiencies in the epidermis of both p53⁺/⁺ and p53⁻/⁻ mice.

Interestingly, there were no increases in gpt MFs at UVB doses above 0.5 kJ/m² in both p53⁺/⁺ and p53⁻/⁻ mice (Fig. 1). These results are consistent with the previous observation that the gpt MF was increased about nine times by UVB irradiation at 0.3 kJ/m², but did not significantly increase more at doses of 0.5–2.0 kJ/m² in wild-type gpt delta mice [Horiguchi et al., 1999]. These results suggest that gpt MFs in the epidermis are saturated at these doses. Ikehata also reported that UVB induction of mutations was suppressed in acute high-dose exposure to the epidermis using Muta™ mice [Ikehata and Ono, 2002]. The suppression occurred even in the absence of p53; therefore, it was not due to p53-dependent antimutagenic effects such as p53-dependent apoptosis. A higher efficiency of DNA repair might be induced at higher UVB doses, or highly

damaged cells might be selectively killed during inflammation induced by UVB irradiation [Ikehata and Ono, 2002]. Whatever the mechanisms are, our results (shown in Fig. 1) raise the possibility that factors other than $p53$ contribute to genome stability in the murine epidermis.

UV-induced mutagenesis is induced by translesion DNA synthesis (TLS) that proceeds across UVB-induced photoproducts such as CPD or 6-4PP [Friedberg et al., 2006]. Specialized DNA polymerases involved in lesion bypass have been identified. These polymerases insert incorrect bases such as dGMP opposite the 3'C of CT sites at a relatively high frequency, thereby generating incorrect nascent DNA sequences during DNA synthesis [Prakash et al., 2005]. This process may rescue stalled DNA synthesis at the lesion and contribute to the completion of whole chromosome replication, but it may induce point mutations as byproducts. DNA polymerase iota, kappa, and zeta may be involved in the error-prone TLS across UV-induced photoproducts [Gueranger et al., 2008; Ziv et al., 2009]. These results shown in Figure 1 suggest that p53 may not be involved in the error-prone TLS across UVB-induced lesions. Although the relationship between p53 and TLS by specialized DNA polymerases has not been thoroughly examined, one report suggests that the mutations on plasmids carrying a benzo[a]pyrene–induced guanine adduct are suppressed by the presence of p53 in mouse embryonic fibroblasts [Avkin et al., 2004]. In the experiments, the mutation frequencies on the plasmids were higher in cells derived from $p53^{-/-}$ mice than in cells from $p53^{+/+}$ mice. Therefore, it was concluded, that p53 suppressed the error-prone nature of specialized DNA polymerases during the bypass processes. However, our results do not support this conclusion, because the MF and UVB-induced mutation spectra were similar between $p53^{-/-}$ and $p53^{+/+}$ mice. The apparent discrepancy may be due to different experimental conditions, for example, DNA lesions, cell types, and detection methods for mutations. Another possibility may be that higher induction of the gpt mutations in $p53^{-/-}$ mice could not be observed because the MFs were already saturated in both $p53^{+/+}$ and $p53^{-/-}$ mice with 0.5 kJ/m^2 irradiation. The effect of p53 may be masked, due to a p53-independent saturation of gpt MFs in this study. Further investigation is needed to examine the relationship between p53 and error rates of TLS by multiple specialized DNA polymerases.

In contrast to the gpt mutations, where no substantial differences were observed between $p53^{+/+}$ and $p53^{-/-}$ mice, Spi$^-$ MF in unirradiated $p53^{-/-}$ mice was 2.5 times higher than that in $p53^{+/+}$ counterparts, although there is no statistical significance because of the small number of n (Table III). Focusing on the specific mutation frequency, in unirradiated $p53^{-/-}$ mice, especially the specific mutation frequencies of large deletions and complex-type rearrangements were significantly higher than those of the large deletions in the $p53^{+/+}$ counterparts (1.58 × 10^{-6} vs. 0.17 × 10^{-6}, $P = 0.04$, Dunnet test) (Fig. 2).

These deletion and complex-type rearrangements are thought to be induced by nonhomologous end-joining during repair of DSB in DNA [Nohmi and Masumura, 2005]. The higher spontaneous mutation frequencies of large deletions and complex-type rearrangements in $p53^{-/-}$ mice suggests that the antigenotoxic effects of $p53$ may be specialized to suppress the mutagenic end-joining process to seal DSB in DNA. This is consistent with previous reports that chromosome alterations, including chromosome loss/duplication and interstitial deletion, are more frequently observed in $p53^{-/-}$ mice compared with $p53^{+/+}$ mice [Shao et al., 2000]. Because of the antimutagenic effects, we expected that the specific Spi$^-$ mutation frequencies for large deletions and complex types would be significantly increased by UVB irradiation in $p53^{-/-}$ mice compared with $p53^{+/+}$ mice. However, the specific mutation frequencies did not increase more than the spontaneous level even after UVB irradiation at doses of 0.5, 1.0, or 2.0 kJ/m^2 in $p53^{-/-}$ mice (Fig. 2). The results suggest the p53-independent antimutagenic mechanisms that suppress gpt mutations (discussed earlier) may also act on cells that have DSB in DNA. Currently, the mechanisms are not known but may be related to inflammation in the skin induced by UVB irradiation [Ikehata and Ono, 2002]. Alternatively, p53 may be positively involved in induction of deletions and complex-type mutations induced by UVB; therefore, there was no increase in the Spi$^-$ mutation frequency in UVB-irradiated $p53^{-/-}$ mice. It is reported that DSB in DNA are induced during the repair of UV photoproducts [Bradley and Taylor, 1981]. It is known that p53 is involved in nucleotide excision repair (NER) [Ford and Hanawalt, 1995, 1997; Smith et al., 2000] and p53 regulates the expression of several NER genes including XPC and DDB2 [Hwang et al., 1999; Adimoolam and Ford, 2002]. Thus, p53 may be involved in the induction of large deletions by regulating the repair of UVB photoproducts. If this is the case, Spi$^-$ large deletions will not be induced in $p53^{-/-}$ mice after UVB irradiation. However, it is possible that the small number of mice and the relatively high background mutation frequency may obscure an effect of UVB in $p53^{-/-}$ mice, because increase in the specific Spi$^-$ mutation frequency caused by UVB is very small even in $p53^{+/+}$ mice. To answer this issue, larger number of mice and improved experimental design may be needed.

The MFs of Spi$^-$ deletions in $p53^{+/+}$ mice increased twofold to fourfold when compared with the control level at UVB doses of 0.5, 1.0, or 2.0 kJ/m^2 (Table III). In a previous study, we observed suppression of UVB-induced large deletions at UVB doses of 1.0, 1.5, or 2.0 kJ/m^2; therefore, the dose–response curve was a bell-shaped one [Horiguchi et al., 2001]. In this study, we did not observe such strong suppression of the Spi$^-$ MF at UVB doses of 1.0 and 2.0 kJ/m^2 (Fig. 2). The apparent discrepancy between the previous and current studies might be due to the different irradia-

Environmental and Molecular Mutagenesis. DOI 10.1002/em

Effects of p53 on Deletions in the Murine Epidermis   251

tion conditions such as dose rates and UVB sources. The dose rate used in this study was 0.3 kJ/m²/min [5 J/m²/s], which is lower than that used in the previous study [17 J/ m²/s]; although, total doses were similar. A handheld UV lamp in a cabinet was used in this study instead of the straight-tube fluorescent lights used in the previous study. The different wavelength distribution of UV from different lamps could also affect the dose responses. When we focus on the larger deletions (greater than 1 kb) and complex types, the specific Spi⁻ MFs of $p53^{+/+}$ mice significantly increased, up to 5.5-fold higher than the control level at 2.0 kJ/m² (0.93×10^{-6} vs. 0.17×10^{-6}) (Fig. 2). However, the specific MF of large deletions and complex types was increased 17-fold in the previous study [Horiguchi et al., 2001]. The lower dose rate used in this study may have caused relatively weaker induction of larger deletions. Dose rate might be an important factor for UVB-induced large deletions driven by DSB and end-joining.

Thirty-nine Spi⁻ large deletions (greater than 1 kb), recovered from both $p53^{+/+}$ and $p53^{-/-}$ mice, were sequenced and are shown in Figure 3. The majority of those deletions have short homologous sequences of 1–4 bp at the junction in both $p53^{+/+}$ and $p53^{-/-}$ mice. The largest deletion size identified was −7,094 bp. The Spi⁻ mutation assays can detect a simultaneous inactivation of both the gam and red genes, which is usually induced by deletions. Because of the size limitation for lambda in vitro packaging reactions (there must be two cos sites separated by 38–51 kb of DNA), deletions up to 10 kb are detectable as Spi⁻ mutations [Nohmi and Masumura, 2004, 2005]. Interestingly, an identical −3,979 bp deletion having a 4 bp (5-TTTA-3′) microhomology at the junction was repeatedly observed in both $p53^{+/+}$ and $p53^{-/-}$ mice. This deletion is not UV-dependent because the same deletion was also independently recovered from the unirradiated epidermis. In the previous study, the same deletion was also observed multiple times in both UVB-irradiated and UVB-unirradiated epidermis (six independent mutations were recovered from 12 mice) [Horiguchi et al., 2001]. In contrast, this deletion was not observed in other tissues, with the exception of 1 identified from the liver out of more than 400 independent Spi⁻ mutants previously sequenced [Yatagai et al., 2002; Nohmi and Masumura, 2004]. This −3,979 bp Spi⁻ deletion may be a hot spot mutation in the epidermis of the mouse. In human skin, a −3,895 bp deletion in mitochondrial DNA was proposed to be a marker for sunlight exposure [Krishnan et al., 2004]. It has a 12-bp microhomology at the junction (5′-CCATACCCCGAA-3′). The relationship between the −3,979 bp deletion in the chromosome DNA of the murine epidermis and the −3,895 bp deletion in the mitochondria DNA in human skin is currently unknown.

Several p53-deficient mouse strains were previously developed to investigate the function of p53 in mutagene-

sis by in vivo mutation detection systems using lacZ, lacI, aprt, etc. [Morris, 2002]. Those mouse models have a common phenotype, a propensity to develop thymic lymphoma. However, the effect of p53 on spontaneous and mutagen-induced mutations has not been thoroughly investigated. In this study, we investigated the role of p53 in spontaneous and UV-induced mutations, including both point mutations and deletions, in the mouse epidermis. The results showed that p53 may suppress spontaneous deletions. This implies that once p53 is inactivated, the mutated cells will display high levels of genome instability, even without additional exposure to sunlight or other environmental mutagens. To better understand p53 functions in mutagenesis in vivo, it is important to further investigate how p53 is involved in several cellular functions such as DNA damage-response and repair pathways.

REFERENCES

Adams WT, Skopek TR. 1987. Statistical test for the comparison of samples from mutational spectra. J Mol Biol 194:391–396.

Adimoolam S, Ford JM. 2002. p53 and DNA damage-inducible expression of the xeroderma pigmentosum group C gene. Proc Natl Acad Sci USA 99:12985–12990.

Aubrecht J, Secretan MB, Bishop AJ, Schiestl RH. 1999. Involvement of p53 in X-ray induced intrachromosomal recombination in mice. Carcinogenesis 20:2229–2236.

Avkin S, Goldsmith M, Velasco-Miguel S, Geacintov N, Friedberg EC, Livneh Z. 2004. Quantitative analysis of translesion DNA synthesis across a benzo[a]pyrene–guanine adduct in mammalian cells: The role of DNA polymerase kappa. J Biol Chem 279:53298–53305.

Bradley MO, Taylor VI. 1981. DNA double-strand breaks induced in normal human cells during the repair of ultraviolet light damage. Proc Natl Acad Sci USA 78:3619–3623.

Brash DE, Rudolph JA, Simon JA, Lin A, McKenna GJ, Baden HP, Halperin AJ, Ponten J. 1991. A role for sunlight in skin cancer: UV-induced p53 mutations in squamous cell carcinoma. Proc Natl Acad Sci USA 88:10124–10128.

Buettner VL, Hill KA, Nishino H, Schaid DJ, Frisk CS, Sommer SS. 1996. Increased mutation frequency and altered spectrum in one of four thymic lymphomas derived from tumor prone p53/Big Blue double transgenic mice. Oncogene 13:2407–2413.

Cariello NF, Piegorsch WW, Adams WT, Skopek TR. 1994. Computer program for the analysis of mutational spectra: Application to p53 mutations. Carcinogenesis 15:2281–2285.

Daya-Grosjean L, Dumaz N, Sarasin A. 1995. The specificity of p53 mutation spectra in sunlight induced human cancers. J Photochem Photobiol B 28:115–124.

Donehower LA, Harvey M, Slagle BL, McArthur MJ, Montgomery CA Jr., Butel JS, Bradley A. 1992. Mice deficient for p53 are developmentally normal but susceptible to spontaneous tumours. Nature 356:215–221.

Ford JM, Hanawalt PC. 1995. Li–Fraumeni syndrome fibroblasts homozygous for p53 mutations are deficient in global DNA repair but exhibit normal transcription-coupled repair and enhanced UV resistance. Proc Natl Acad Sci USA 92:8876–8880.

Ford JM, Hanawalt PC. 1997. Expression of wild-type p53 is required for efficient global genomic nucleotide excision repair in UV-irradiated human fibroblasts. J Biol Chem 272:28073–28080.

Friedberg EC, Walker GC, Siede W, Wood RD, Schultz RA, Ellenberger T. 2006. DNA Repair and Mutagenesis. 2nd ed. Washington, DC: ASM press. 1118 p.

Gueranger Q, Stary A, Aoufouchi S, Faili A, Sarasin A, Reynaud CA, Weill JC. 2008. Role of DNA polymerases eta, iota and zeta in UV resistance and UV-induced mutagenesis in a human cell line. DNA Repair (Amst) 7:1551–1562.

Hauser J, Seidman MM, Sidur K, Dixon K. 1986. Sequence specificity of point mutations induced during passage of a UV-irradiated shuttle vector plasmid in monkey cells. Mol Cell Biol 6:277–285.

Horiguchi M, Masumura K, Ikehata H, Ono T, Kanke Y, Sofuni T, Nohmi T. 1999. UVB-induced gpt mutations in the skin of gpt delta transgenic mice. Environ Mol Mutagen 34:72–79.

Horiguchi M, Masumura K, Ikehata H, Ono T, Kanke Y, Nohmi T. 2001. Molecular nature of ultraviolet B light-induced deletions in the murine epidermis. Cancer Res 61:3913–3918.

Hsia HC, Lebkowski JS, Leong PM, Calos MP, Miller JH. 1989. Comparison of ultraviolet irradiation-induced mutagenesis of the lacI gene in Escherichia coli and in human 293 cells. J Mol Biol 205:103–113.

Hwang BJ, Ford JM, Hanawalt PC, Chu G. 1999. Expression of the p48 xeroderma pigmentosum gene is p53-dependent and is involved in global genomic repair. Proc Natl Acad Sci USA 96:424–428.

Ikehata H, Ono T. 2002. Mutation induction with UVB in mouse skin epidermis is suppressed in acute high-dose exposure. Mutat Res 508:41–47.

Ikehata H, Aiba S, Ozawa H, Ono T. 2001. Thermolysin improves mutation analysis in skin epidermis from ultraviolet light-irradiated Muta mouse. Environ Mol Mutagen 38:55–58.

Ikehata H, Masuda T, Sakata H, Ono T. 2003. Analysis of mutation spectra in UVB-exposed mouse skin epidermis and dermis: Frequent occurrence of C→T transition at methylated CpG-associated dipyrimidine sites. Environ Mol Mutagen 41:280–292.

Ikehata H, Nakamura S, Asamura T, Ono T. 2004. Mutation spectrum in sunlight-exposed mouse skin epidermis: Small but appreciable contribution of oxidative stress-mediated mutagenesis. Mutat Res 556:11–24.

Jacks T, Remington L, Williams BO, Schmitt EM, Halachmi S, Bronson RT, Weinberg RA. 1994. Tumor spectrum analysis in p53-mutant mice. Curr Biol 4:1–7.

Krishnan KJ, Harbottle A, Birch-Machin MA. 2004. The use of a 3895 bp mitochondrial DNA deletion as a marker for sunlight exposure in human skin. J Invest Dermatol 123:1020–1024.

Lambert IB, Singer TM, Boucher SE, Douglas GR. 2005. Detailed review of transgenic rodent mutation assays. Mutat Res 590:1–280.

Miller JH. 1985. Mutagenic specificity of ultraviolet light. J Mol Biol 182:45–65.

Morris SM. 2002. A role for p53 in the frequency and mechanism of mutation. Mutat Res 511:45–62.

Nishino H, Knoll A, Buettner VL, Frisk CS, Maruta Y, Haavik J, Sommer SS. 1995. p53 wild-type and p53 nullizygous Big Blue transgenic mice have similar frequencies and patterns of observed mutation in liver, spleen and brain. Oncogene 11:263–270.

Nohmi T. 2007. Novel DNA polymerases and novel genotoxicity assays. Genes Environ 29:75–88.

Nohmi T, Masumura K. 2004. Gpt delta transgenic mouse: A novel approach for molecular dissection of deletion mutations in vivo. Adv Biophys 38:97–121.

Nohmi T, Masumura K. 2005. Molecular nature of intrachromosomal deletions and base substitutions induced by environmental mutagens. Environ Mol Mutagen 45:150–161.

Nohmi T, Katoh M, Suzuki H, Matsui M, Yamada M, Watanabe M, Suzuki M, Horiya N, Ueda O, Shibuya T, Ikeda H, Sofuni T. 1996. A new transgenic mouse mutagenesis test system using Spi⁻ and 6-thioguanine selections. Environ Mol Mutagen 28:465–470.

Nohmi T, Suzuki T, Masumura K. 2000. Recent advances in the protocols of transgenic mouse mutation assays. Mutat Res 455:191–215.

Prakash S, Johnson RE, Prakash L. 2005. Eukaryotic translesion synthesis DNA polymerases: Specificity of structure and function. Annu Rev Biochem 74:317–353.

Purdie CA, Harrison DJ, Peter A, Dobbie L, White S, Howie SE, Salter DM, Bird CC, Wyllie AH, Hooper ML. 1994. Tumour incidence, spectrum and ploidy in mice with a large deletion in the p53 gene. Oncogene 9:603–609.

Sands AT, Suraokar MB, Sanchez A, Marth JE, Donehower LA, Bradley A. 1995. p53 deficiency does not affect the accumulation of point mutations in a transgene target. Proc Natl Acad Sci USA 92:8517–8521.

Shao C, Deng L, Henegariu O, Liang L, Stambrook PJ, Tischfield JA. 2000. Chromosome instability contributes to loss of heterozygosity in mice lacking p53. Proc Natl Acad Sci USA 97:7405–7410.

Shibata A, Masutani M, Nozaki T, Kamada N, Fujihara H, Masumura K, Nakagama H, Sugimura T, Kobayashi S, Suzuki H, Nohmi T. 2003. Improvement of the Spi⁻ assay for mutations in gpt delta mice by including magnesium ions during plaque formation. Environ Mol Mutagen 41:370–372.

Smith ML, Ford JM, Hollander MC, Bortnick RA, Amundson SA, Seo YR, Deng CX, Hanawalt PC, Fornace AJ Jr. 2000. p53-mediated DNA repair responses to UV radiation: Studies of mouse cells lacking p53, p21, and/or gadd45 genes. Mol Cell Biol 20:3705–3714.

Tsukada T, Tomooka Y, Takai S, Ueda Y, Nishikawa S, Yagi T, Tokunaga T, Takeda N, Suda Y, Abe S. 1993. Enhanced proliferative potential in culture of cells from p53-deficient mice. Oncogene 8:3313–3322.

Yatagai F, Kurobe T, Nohmi T, Masumura K, Tsukada T, Yamaguchi H, Kasai-Eguchi K, Fukunishi N. 2002. Heavy-ion-induced mutations in the gpt delta transgenic mouse: Effect of p53 gene knockout. Environ Mol Mutagen 40:216–225.

Ziegler A, Leffell DJ, Kunala S, Sharma HW, Gailani M, Simon JA, Halperin AJ, Baden HP, Shapiro PE, Bale AE. 1993. Mutation hotspots due to sunlight in the p53 gene of nonmelanoma skin cancers. Proc Natl Acad Sci USA 90:4216–4220.

Ziv O, Geacintov N, Nakajima S, Yasui A, Livneh Z. 2009. DNA polymerase zeta cooperates with polymerases kappa and iota in translesion DNA synthesis across pyrimidine photodimers in cells from XPV patients. Proc Natl Acad Sci USA 106:11552–11557.

Structural insight into dynamic bypass of the major cisplatin-DNA adduct by Y-family polymerase Dpo4

Jimson HY Wong[1], Jessica A Brown[2],
Zucai Suo[2], Paul Blum[3], Takehiko Nohmi[4]
and Hong Ling[1],*

[1]Department of Biochemistry, University of Western Ontario, London, Ontario, Canada, [2]Department of Biochemistry, The Ohio State University, Columbus, OH, USA, [3]School of Biological Sciences, University of Nebraska, Lincoln, NE, USA and [4]Division of Genetics and Mutagenesis, National Institute of Health Sciences, Setagaya-ku, Tokyo, Japan

Y-family DNA polymerases bypass Pt-GG, the cisplatin-DNA double-base lesion, contributing to the cisplatin resistance in tumour cells. To reveal the mechanism, we determined three structures of the Y-family DNA polymerase, Dpo4, in complex with Pt-GG DNA. The crystallographic snapshots show three stages of lesion bypass: the nucleotide insertions opposite the 3'G (first insertion) and 5'G (second insertion) of Pt-GG, and the primer extension beyond the lesion site. We observed a dynamic process, in which the lesion was converted from an open and angular conformation at the first insertion to a depressed and nearly parallel conformation at the subsequent reaction stages to fit into the active site of Dpo4. The DNA translocation-coupled conformational change may account for additional inhibition on the second insertion reaction. The structures illustrate that Pt-GG disturbs the replicating base pair in the active site, which reduces the catalytic efficiency and fidelity. The in vivo relevance of Dpo4-mediated Pt-GG bypass was addressed by a dpo-4 knockout strain of Sulfolobus solfataricus, which exhibits enhanced sensitivity to cisplatin and proteomic alterations consistent with genomic stress.

Introduction

All living organisms are hindered by DNA damage that generates replication-blocking lesions in DNA. Therefore, there are DNA repair mechanisms to remove lesions and damage-tolerance mechanisms for replication through le-

*Corresponding author. Department of Biochemistry, University of Western Ontario, London, Ontario, Canada N6A 5C1.
Tel.: +1 519 661 3557; Fax: +1 519 661 3175;
E-mail: hling4@uwo.ca

sions. Translesion synthesis (TLS) is a DNA damage-tolerance mechanism that uses specialized DNA polymerases (e.g. members of the Y-family) to replicate damaged DNA (Friedberg et al, 2002; Lehmann, 2002). TLS has an important function in cell survival of DNA damage and is highly conserved from bacteria to humans (Goodman, 2002).

cis-Diamminedichloroplatinum (II) (cisplatin) is a widely used chemotherapeutic agent that covalently modifies DNA to block DNA replication in rapidly dividing tumour cells (Davidson et al, 1975; Lippert, 1999). Cisplatin reacts with the N7 atoms of adjacent guanine (G) bases to create a 1,2-intrastrand covalent linkage, cis-Pt-1,2-d(GpG) (Pt-GG) (Supplementary Figure S1), which is the major cisplatin adduct, representing ~65% of the cisplatin-DNA adducts in cells (Pinto and Lippard, 1985; Sherman et al, 1985; Coll et al, 1990; Takahara et al, 1995; Jamieson and Lippard, 1999). By inhibiting DNA synthesis, cisplatin-DNA adducts slow cell division, possibly activating programmed cell death or apoptosis (Eastman, 1990; Cohen and Lippard, 2001). Thus, cisplatin is an effective anti-cancer drug, especially for cancers of the testis, ovary, bladder, head, neck, and lung. TLS and DNA repair mechanisms have contributed to acquired and intrinsic cisplatin resistance, thereby limiting the drug's application and contributing to cancer recurrence (Siddik, 2003; Zorbas and Keppler, 2005). Cells have been shown to have the ability to replicate past cisplatin-DNA adducts (Gibbons et al, 1991; Mamenta et al, 1994; Vaisman et al, 1998). Some translesional DNA polymerases can bypass cisplatin-DNA adducts (Hoffmann et al, 1995, 1996; Vaisman and Chaney, 2000; Vaisman et al, 2000; Albertella et al, 2005) and are overexpressed in tumour cells (Canitrot et al, 1998; Bergoglio et al, 2001). In addition, TLS is increased in the drug-resistant cells (Gibbons et al, 1991; Mamenta et al, 1994), strongly suggesting that TLS is correlated with resistance to cisplatin (Richon et al, 1987; Gibbons et al, 1991; Roush et al, 1998). Thus, TLS is considered to be one of the main mechanisms of cisplatin resistance in cancer treatment (Vaisman et al, 1998; Suo et al, 1999).

Most of the specialized translesion DNA polymerases are members of the Y-family. These DNA polymerases have a spacious active site that can accommodate bulky and distorted DNA lesions (Yang and Woodgate, 2007). However, a result of the expansion of these enzymes' functional repertoire and substrate specificity is that Y-family DNA polymerases replicate DNA with a higher error frequency (McCulloch and Kunkel, 2008). Hence, although Y-family DNA polymerases promote damage tolerance and cell survival, they also contribute to enhanced cellular mutagenesis. Human Y-family DNA polymerase η bypasses Pt-GG in a relatively efficient and error-free manner (Vaisman et al, 2000; Albertella et al, 2005). Recently, a structural study on yeast DNA polymerase η (yPolη) in complex with Pt-GG DNA provides the first glimpse of Pt-GG lesion bypass during

the base insertion stages (Alt *et al*, 2007). The canonical dCTP is the preferred nucleotide inserted by yPolη opposite both the 3′ and 5′G base of a Pt-GG cross-link (Alt *et al*, 2007). However, the structures do not show dCTP insertion opposite the 5′G base (Alt *et al*, 2007). Also notable, the yPolη structures do not have the whole double-base Pt-GG adduct accommodated within the active site. Further study is essential to answer the key question of how the bulky/angular-shaped Pt-GG adduct is translocated through the active site of a DNA polymerase during the lesion bypass.

We report three crystal structures of a model Y-family DNA polymerase, DNA polymerase IV (Dpo4) from *Sulfolobus solfataricus*, in complex with Pt-GG DNA at 2.9, 1.9, and 2.0 Å resolution, respectively. During the TLS process, DNA polymerases perform two fundamental steps: nucleotide incorporation opposite the damaged DNA base(s) and extension past the lesion. Our three ternary structures encompassed these pertinent steps of TLS: dCTP insertion opposite the 3′ and 5′G bases of the Pt-GG adduct and correct dATP insertion for the extension step immediately downstream of the lesion. To support the structural results, we have investigated the bypass of Pt-GG catalysed by Dpo4 in solution. In addition, the *in vivo* function of Dpo4 was addressed for the first time through the construction and analysis of a *S. solfataricus* cell line harbouring a loss of function mutation leading to deficiency of this organism's only lesion bypass polymerase.

Results

Overall structures of the Dpo4–DNA–dNTP ternary complexes

We have co-crystallized Dpo4 with template DNA containing Pt-GG with dNTPs against the 3′G (GG1), the 5′G (GG2) of Pt-GG, and the T base 5′ to the lesion (GG3), respectively (Figure 1). All three of our Dpo4–Pt-GG-DNA–dNTP ternary structures (GG1, GG2, and GG3) share a common crystal form, with one complex per asymmetric unit (Table I). The overall ternary complexes are essentially identical to the type I complex and other active Dpo4 structures (Ling *et al*, 2001, 2003, 2004a, b). The type I structure is the first Dpo4–DNA–dNTP ternary complex structure with normal nucleotide incorporation and represents a common active form of Dpo4, as well as most other Y-family DNA polymerases (Supplementary Figure S2). In this common active form, the finger domain is in a closed conformation packing against the catalytic palm domain and contacts the replicating base pair in the active site. Structural superposition of the three complex structures and the type I shows that the Dpo4 remains an identical conformation with root mean square deviations (r.m.s.d.) <0.5 Å on all Cα atoms, pair wisely. The closed finger conformation has been observed in other Dpo4 structures, which were solved in different crystal forms (Ling *et al*, 2004a; Rechkoblit *et al*, 2006; Wong *et al*, 2008). Therefore, the closed finger conformation in our current structures is independent of crystal packing.

All three GG complexes have the same 18-mer DNA template that contains a site-specific Pt-GG adduct at the 14th and 15th positions from the DNA's 3′ end (Figure 2). Three different 13-mer primers were designed to generate DNA substrates for nucleotide insertions opposite or extension beyond the Pt-GG adduct in the template strand (Figure 2). Dideoxy-terminated primers (ddC or ddG) were

used to trap the ternary complexes in the desired reaction stages during TLS of Pt-GG. The single-stranded template residues 5′ to the adduct are completely disordered in both insertion structures GG1 and GG2. The incoming nucleotides in the three GG complexes are superimposed well with the dNTP from the ternary complexes of Dpo4 and undamaged DNA (Figure 1D and E) (Ling *et al*, 2004a; Vaisman *et al*, 2005), showing that Dpo4 maintains the incoming dNTP in a similar position and orientation in the active site, regardless of the DNA template position. Thus, the structural differences are localized at the site of the DNA adduct in the template strand. The Pt-GG adduct conformation is varied in the three structures, which deviates from the low-energy Pt-GG conformation as described by the ideal torsion angles α and β (Supplementary Table S1). The torsion angle α defines the degree of Pt out-of-plane bending (C8-N7-C5-Pt, an ideal value of 180° for in-plane conformation), and β represents the torsion angle between the G base planes and the Pt-coordination plane (C8-N7-Pt-*cis*N, an ideal value of 90°) (Yao *et al*, 1994). The torsion angles in our three structures deviate up to 10° beyond the range established from the single *cis*-Pt-GG adduct crystal structures (Sherman *et al*, 1985) and the protein-free Pt-GG adducted DNA structures (Takahara *et al*, 1995), and thus are further off from the ideal low-energy state (Yao *et al*, 1994). The DNA helices bound by Dpo4 are in a straight form with bending angles <18° over the 12-bp helical region, which is in contrast to the curved protein-free Pt-GG adducted DNA (Takahara *et al*, 1995) (Figure 3). It seems that the helical DNA geometry and the protein binding place additional strains to distort the Pt-GG adduct from its low-energy conformations. The distances between the Pα atoms of the incoming nucleotides and the C3′ atoms at the 3′ end of the primer strands are ~5 Å, a catalytically competent distance, in the presence of two catalytic divalent metal ions in all three structures (Figure 1).

GG1: dCTP insertion opposite the 3′G of Pt-GG (first insertion)

The GG1 structure represents the first insertion stage of Pt-GG lesion bypass. The incoming dCTP is poised for insertion opposite the 3′G base of the Pt-GG adduct at the active site. The position of the platinum atom is identified by an anomalous difference peak, which is shifted into the DNA major groove (Figure 1A). Moreover, the finger domain in the closed conformation wedges between two Pt-coordinated G bases and blocks the 5′G from entering the active site completely (Figure 2A). Thus, the 5′ base of Pt-GG is in close contact with the finger domain and is positioned outside of the active site. As the 3′G and 5′G are covalently linked through cisplatin, the 3′G base is dragged into the major groove by the 5′G, thereby preventing the 3′G from resting in the optimal template position of an undamaged DNA template (Figure 1). Compared with an undamaged DNA template, the 3′G is shifted 4.0 Å towards the major groove (Figure 1A, D, and E). The DNA helix in GG1 keeps a straight form, and the adduct is not completely included into the helical structure yet. In the first insertion structure (GG1), Pt-GG possesses a large roll angle of 135° between the 5′G and 3′G bases due to its close contacts with the finger domain (Figure 2A). In this open angular conformation, the Pt atom is out of plane of the bases with the α angles deviated by 8–37°, and the Pt-
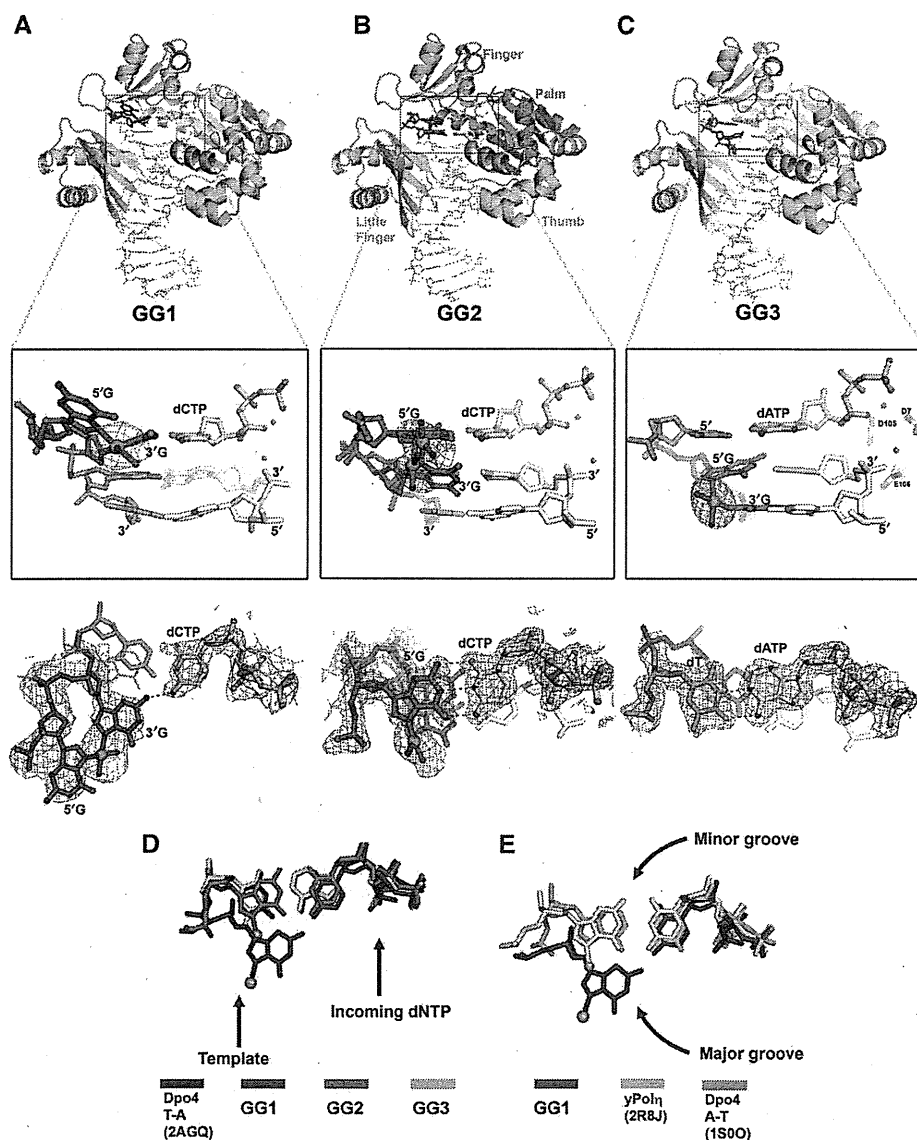
Figure 1 The structures of the GG1 (A), GG2 (B), and GG3 (C) Dpo4–DNA–dNTP ternary complexes. The finger, palm, thumb, and little finger domains distinguished by their respective colours in (B). The Pt-GG lesioned template is represented in magenta, with the platinum atom shown as a cyan ball. The zoomed in boxes of the active site are covered with the Pt-anomalous maps (5 σ) in orange. The catalytic residues are shown in the middle panel of Figure 1C, which present invariantly in all three structures. There are two base conformers of Pt-GG in (B), with each Pt atom at 0.5 occupancy. The top views of the replicating base pairs are covered by a blue 2Fo-Fc maps contoured to 1.0 σ at 2.9, 1.9, and 2.0 Å resolution, respectively. The A-T pair in green sticks superimposed with GG1 (A) is taken from a Dpo4–DNA–dNTP complex structure (PDB: 1SOO), which depicts the regular position of an undamaged purine-pyrimidine base pair in the Dpo4 active site. The grey nucleotide in (A, middle box) is a ghost model for the 3′ primer base that is disordered in GG1. The green spheres are Ca^{2+} ions. (D) A top view comparison of the GG1 (blue), GG2 (red), and GG3 (cyan) replicating base pairs with an undamaged pyrimindine-purine (T-A) replicating base pair (2AGQ, black). (E) A top view comparison of the Dpo4 GG1 base pair with the yeast pol η GG1 (2R8J, beige) and an undamaged purine-pyrimidine (A-T) (1SOO, green) replicating base pairs.

coordination plane off the ideal β torsion by 22–60° (Supplementary Table S1). The conformation of Pt-GG in GG1 are dramatically distorted due to the position of the finger domain wedging between the two G bases. In contrast, the Pt-GG adducts in the open ypolη structure are very close to the ideal model with roll angles of ~90°, α angles of <5° from ideal 180°, and β angles within 30° from ideal 90° (Alt *et al*, 2007).

The Pt-GG adduct outside of the active site is not stabilized by base stacking and Watson–Crick (WC) base pairing,

leading to a disturbed template (poor density, Figure 1A) with high B-factors. The 3′G base of the Pt-GG adduct shifted into the major groove loses base stacking with the upstream −1 template base. Furthermore, the shifted 3′G base does not form a WC base pair with the incoming dCTP that is in the same position as the incoming dNTPs in the structures 2AGQ and 1SOO (Figure 1A, D, and E) which exhibit the regular position of an undamaged base pair in the Dpo4 active site (Ling *et al*, 2004a; Vaisman *et al*, 2005). Only one H-bond is maintained in the misaligned base pair, which is between two

Table I Data collection and refinement statistics

	GG1	GG2	GG3
Data collection			
Space group	P2$_1$2$_1$2	P2$_1$2$_1$2	P2$_1$2$_1$2
Cell dimensions			
a, b, c (Å)	98.6, 101.2, 52.4	98.2, 103.2, 52.3	99.2, 103.7, 52.0
Resolution (Å)[a]	50.0–2.90 (3.00–2.90)	50.0–1.93 (1.96–1.93)	50.0–2.00 (2.03–2.00)
R_{sym} or R_{merge}	0.061 (0.670)	0.066 (0.474)	0.087 (0.722)
$I/\sigma I$	22.0 (2.2)	27.4 (2.35)	24.5 (2.5)
Completeness (%)	98.6 (99.4)	99.2 (91.6)	99.8 (95.3)
Redundancy	3.5 (3.4)	7.6 (5.3)	8.0 (6.2)
Refinement			
Resolution (Å)	45.0–2.90	27.6–1.93	29.0–2.00
No. of reflections	12009	40552	36729
R_{work}/R_{free}	0.285/0.309	0.243/0.261	0.224/0.235
No. of atoms			
Protein	2743	2728	2714
DNA	586	636	656
Ligand/ion	22	3	4
Water	49	307	258
B-factors			
Protein	60.4	32.8	34.0
DNA	76.3	34.1	38.7
Ligand/ion	58.8	26.1	36.8
Water	55.0	42.6	41.2
R.m.s. deviations			
Bond lengths (Å)	0.009	0.008	0.015
Bond angles (deg)	1.73	1.71	1.64

[a]Values in parentheses are for highest-resolution shell.

NH$_2$ groups from the 3'G base (N2) of Pt-GG and the base (N4) of dCTP (Figure 1A). Noticeably, the H-bond is a symmetrical H-bond that is of greater-than-normal strength (Cleland *et al*, 1998; Kraut *et al*, 2006; Lone *et al*, 2007). The symmetric H-bond is formed between donor and acceptor atoms from identical NH$_2$ groups that have equal pKa values (Supplementary Figure S1). The unique H-bond provides a structural basis for the preference of dCTP insertion opposite the lesion in the primer extension assays (see *In Vitro* Studies). Other bases, such as A, T, and G, do not have such a NH$_2$ group as found in C, to form a symmetrical and stronger H-bond with the major groove-shifted 3'G of Pt-GG in the GG1 structure. Therefore, dCTP is the preferred nucleotide incorporated at the 3'G of Pt-GG, despite the WC base pair being disrupted by the covalent modification of the DNA template base.

The structural perturbation within the DNA template strand is propagated to the 3' end of the primer strand at the template-primer junction. The template C base upstream (3') to the Pt-GG lesion loses the base stacking interaction with the 3'G and is over wound by 12° (Figure 2A). Consequently, the 3'G base of the primer as a base pairing partner for the over wound template C base is disordered as the electron density for the G base completely disappears (Figure 1A; Supplementary Figure S3). The disordered primer end likely causes template-primer misalignment, which leads to frameshift mutations. The disordering observed in GG1 is supported by a single deletion by Dpo4 in our solution studies (see *In vitro* Studies below). The incoming dCTP resides at a catalytically competent position with the distance between its Pα and the 3' end of the primer being 5.6 Å (Figures 1A and 2A), as the backbone of the primer strand is still structured at its 3' end (Supplementary Figure S3). However, base stacking

interactions were lost between the incoming nucleotide and the disordered primer base, which makes the ternary complex less stable than the structures with undamaged DNA. The lesion template-induced disordering of 3' terminal primer end would contribute to the impaired catalytic capability of Dpo4 at this stage (see *In vitro* studies).

GG2: dCTP incorporation against the 5'G of Pt-GG (second insertion)

An incoming dCTP is inserted opposite the 5'G of Pt-GG in the GG2 ternary complex that captures the second insertion stage. For the first time, this structure shows the two G bases of Pt-GG entering a polymerase active site simultaneously (Figure 1B). The adduct is in two alternate conformations (GG2a and GG2b) that are tilted about 10° with respect to each other (Figures 2B, C, and 3A). In the anomalous difference map, two discrete peaks show the alternate positions of the Pt atom (Figure 1B). The presence of the alternate conformers agrees with the bulged electron density map around the Pt-GG adduct (Figure 3A). The DNA helix keeps a straight form as observed in other Dpo4–DNA complex structures (Figure 3B). As it translocated into the active site (Figure 2E), the adduct adopts depressed roll (ρ) angles as low as 22° between the cross-linked bases, substantially less than ~90° roll angles observed in a single Pt-GG (Sherman *et al*, 1985). In other words, the roll angle is converted from 135° in GG1 to 22° in GG2 to fit Pt-GG into the active site (Figure 2E). Accordingly, the α and β torsion angles of Pt-GG deviate up to 60° from the low-energy conformation (Supplementary Table S2). A reduction in the roll angles and use of alternate conformations make the cross-linked Pt-GG more compatible with the base stacking system of a straight helix (Figure 3B). This set-up
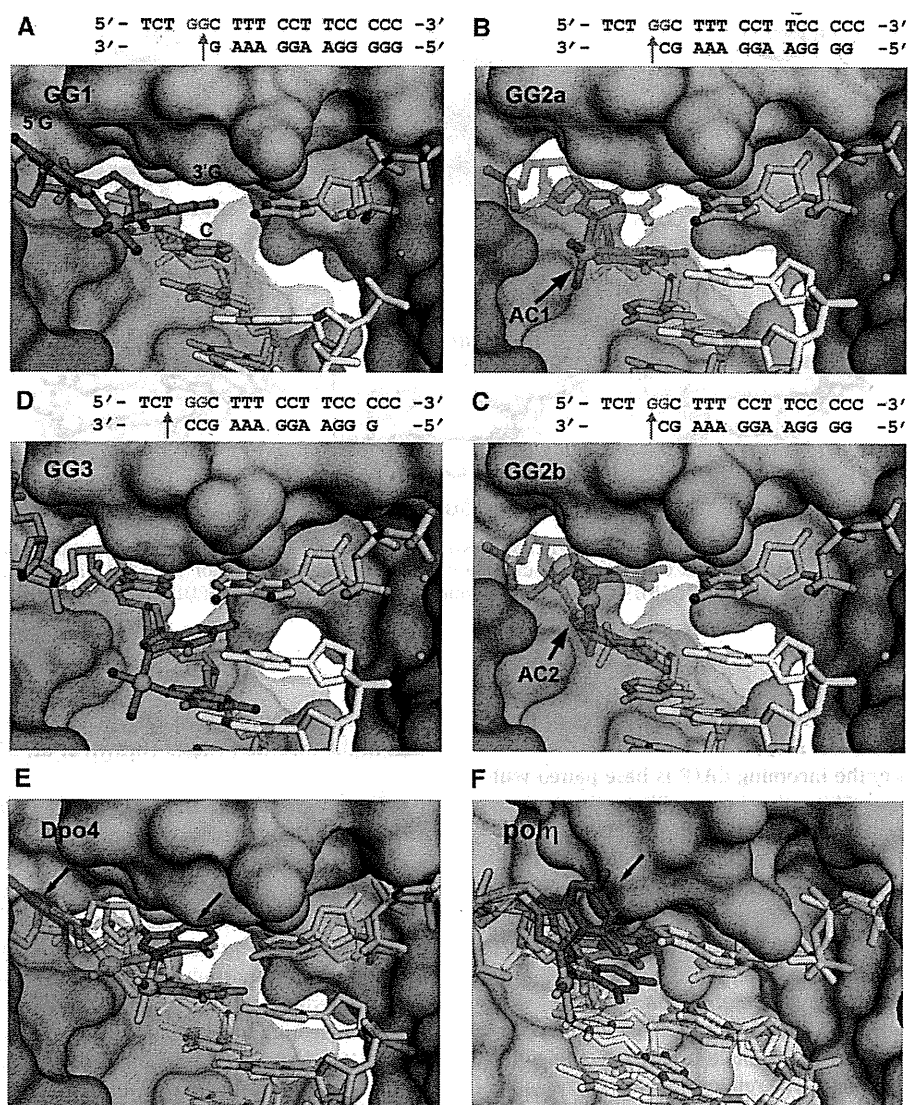
A

5'- TCT GGC TTT CCT TCC CCC -3'
3'-   ↑G AAA GGA AGG GGG -5'

B

5'- TCT GGC TTT CCT TCC CCC -3'
3'-   ↑CG AAA GGA AGG GG -5'

D

5'- TCT GGC TTT CCT TCC CCC -3'
3'- ↑ CCG AAA GGA AGG G   -5'

C

5'- TCT GGC TTT CCT TCC CCC -3'
3'-   ↑CG AAA GGA AGG GG -5'

E

F

Figure 2 Pt-GG adducts in the active sites of Dpo4 and ypolη. All panels are close-up views of the enzyme active sites where the finger domain is in cyan. The platinum (Pt) atom is shown as a cyan ball. The DNA is shown as stick-balls, with the template strand in orange and the primer strand in yellow. The sequences of the template/primer DNA in the complexes are shown on the tops of panels (A–D), cross-linked G bases are in red. The arrows indicate the incoming dNTP positions. (A) GG1, where dCTP (pink) is paired opposite the 3'G of Pt-GG (dark pink). (B, C) GG2, two alternate conformations of GG2 (translucent pink, GG2a in (B), GG2b in (C)), where dCTP (pink) is paired opposite the 5'G of Pt-GG. (D) GG3, where dATP is paired with the T base that is 5' to the Pt-GG lesion. (E) Superposition of the GG1 (semi-transparent, left side) and GG2 (solid, right) structures of Dpo4, where DNA is shown as grey sticks with the 5'G of Pt-GG is in red with arrows, and the 3'G is in blue. The Pt-GG adduct is translocated in different positions and shows different conformations in the two structures. (F) Superposition of the same reaction stage complexes of ypolη with the same colour scheme as (E). In ypolη (F), the Pt-GG adduct remains in a similar position with the 5'G bases (red bases with an arrow) superimposed well in both reaction stages, no translocation of Pt-GG occurs.

reduces the perturbation caused by an angular adduct on the DNA helical structure and helps the lesion fit into the active site.

The 5'G of Pt-GG forms a WC base pair with the incoming dCTP in the active site (Figure 1B). The replicating base pair is in the regular position and superimposed well with the undamaged DNA replicating base pairs (Figure 1D). The finger domain is in contact with the replicating base pair (Figure 2B and C), which makes the 5'G base of Pt-GG less tilted from the base stacking system than the 3'G base (Figure 3A and B). The α-phosphate of dCTP was 4.5 Å from the C3' atom of ddC at the 3' end of the primer strand, indicating that

the incoming nucleotide is poised for catalysis. The WC base paired replicating base pair explains the preference of dCTP over other dNTPs in the second insertion step (see In Vitro Studies). However, the alternate conformations and the geometric strain on the angular Pt-GG bases reflect a high energetic state for the GG2 complex, which contributes to the reduced nucleotide incorporation in the second insertion (Brown et al, 2008). Overall, the energetically unfavourable adduct conformation and the Pt-GG conformational conversion associated entropy cost may account for the lowest efficiency of nucleotide incorporation in the second insertion during the Pt-GG bypass (Brown et al, 2008).
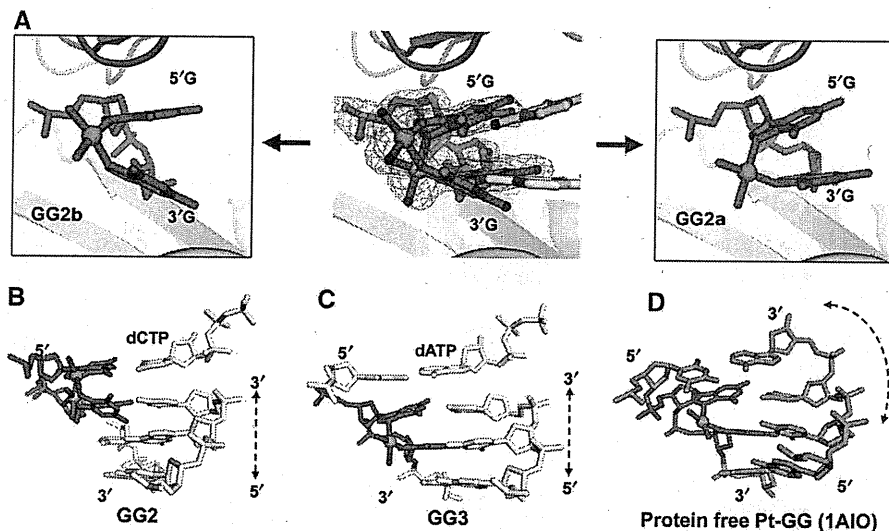
Figure 3 Pt-GG conformations and helical DNA structures in the presence or absence of Dpo4 enzyme. (A) Alternate conformations of Pt-GG in the GG2 structure. The alternate Pt atom corresponds to discrete bulges of electron density for the 1.9 Å 2Fo-Fc map contoured at 1σ. (B–D) Comparison of the DNA helices in GG2 (B), GG3 (C), and enzyme-free Pt-GG structure (D) (PDB: 1AIO). The Pt-GG in the enzyme-free DNA induces a bend in the DNA helix.

GG3: nucleotide incorporation after the bypass of the Pt-GG adduct (extension step)

In the GG3 structure, the incoming dATP is base paired with the template T base 5′ to the lesion, illustrating primer extension after the Pt-GG lesion (Figure 1C). The Pt-GG adduct is in a depressed conformation with roll angle of 26° to fit into the straight DNA helix in GG3 (Figures 1C and 2D). As the Pt-GG adduct has moved out of the active site in GG3, the adduct is less strained than the adduct in GG2. The α/β torsion angles of Pt-GG in GG3 are a few degrees less distorted from the low-energy conformation than the lesion in GG2 (Supplementary Table S1). A single anomalous peak shows one position of the platinum atom with a well-defined lesion structure (Figure 1C). The replicating base pair exhibits normal WC base pairing in the active site and is superimposed well with the standard replicating base pair in Dpo4 (Figure 1D). The replicating base pair has the template T and dATP in plane, which is confined by the closed finger domain (Figure 2D). However, the base pair (5′G*:C) beneath the replicating base pair is significantly disrupted due to the tilted orientation of the 5′G base from the angular Pt-GG (Figure 3C). The G base buckles 15° and propels 18° from the base pair partner C base (Figures 1C and 3C). The disturbed base pair is not in the active site as a replicating base pair, so the structural distortion appears to be less disruptive to DNA replication as in GG1 and GG2. The crosslinked G base 18° tilting from the template T base in the active site, however, does disturb the replicating base pair as a poor stacking partner (Figure 3C), which corresponds to the nucleotide incorporation reduction observed in the extension stage (Brown *et al*, 2008). Overall, the GG3 complex structure was similar to that of Dpo4 with undamaged DNA (Ling *et al*, 2001, 2003, 2004a,b; Vaisman *et al*, 2005), which maintains an ideal WC base paring for the replicating base pair in the active site (Figure 1C). The DNA structural disturbance caused by Pt-GG in GG3 is mainly on the base pair which has moved out of the active site. Therefore, the

Pt-GG lesion would impair catalysis less in the extension than that in the insertion stages (Brown *et al*, 2008).

In vitro studies of Pt-GG bypass by Dpo4

To examine Dpo4-mediated bypass of Pt-GG under conditions similar to crystal formation, we performed a running start assay with a short heteroduplex 10/18-mer at 23°C (Supplementary Figure S4). The template was modified at positions 14 and 15 with cisplatin, identical to the one used for crystallographic studies. There was significant accumulation of intermediate products (13- and 14-mers) corresponding to nucleotide incorporation opposite the two G bases of the Pt-GG adduct (13-mer is pre-first insertion, 14-mer is pre-second insertion), identical to the observation for the assays with longer substrates at 37°C (Brown *et al*, 2008). Thus, these results support our structural observations that the Pt-GG disturbs the replicating base pair in the active site in GG1 and GG2, which causes Dpo4 to pause during nucleotide incorporation opposite the Pt-GG adduct. Interestingly, the full product is 1 nt shorter in the lesion DNA than that of the undamaged DNA in the control panel (Supplementary Figure S4). The shorter product is likely caused by −1 frameshift mutation due to template-primer misalignment. The misalignment has been observed in the Dpo4 structures in which template-primer junctions are disturbed in the active site (Ling *et al*, 2001, 2004a; Bauer *et al*, 2007). The single deletion observed in our running start assay supports the template-primer junction instability caused by the Pt-GG adduct, such as the disordered 3′ end primer end in GG1. The frameshift mutations has been also observed in Pt-GG replication by human DNA polymerase η *in vitro* (Bassett *et al*, 2002), which may be a common mechanism in TLS of Pt-GG.

To confirm that WC base paring in the active site is disturbed by the Pt-GG lesion in solution, we performed the nucleotide incorporation assays using individual dNTP nucleotides (Figure 4). Less product formation was observed
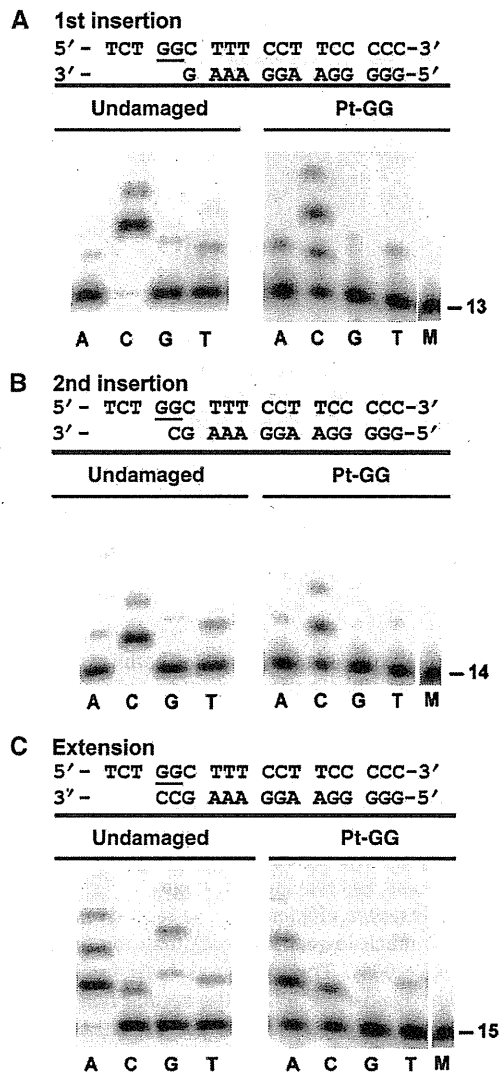
A 1st insertion

```
5' - TCT GGC TTT CCT TCC CCC-3'
3' -     G AAA GGA AGG GGG-5'
```


B 2nd insertion

```
5' - TCT GGC TTT CCT TCC CCC-3'
3' -    CG AAA GGA AGG GGG-5'
```


C Extension

```
5' - TCT GGC TTT CCT TCC CCC-3'
3' -   CCG AAA GGA AGG GGG-5'
```


Figure 4 Specificity of Dpo4-mediated nucleotide incorporation was tested for the (A) GG1 (first insertion), (B) GG2 (second insertion), and (C) GG3 (extension) reaction stages with a dNTP (A, C, G, or T). M represents the marker for the primer strand. In each panel, nucleotide incorporation assays were terminated after 10 min for undamaged DNA (left) and after 60 min for Pt-GG DNA (right).

when Dpo4 was replicating cisplatin-DNA compared with undamaged DNA (Figure 4), supporting the structural disturbance of the replicating base pairs in the GG1, GG2, and GG3 structures. During Pt-GG lesion bypass, Dpo4 preferentially inserted a canonical dCTP opposite the Pt-GG lesion in the following order: dCTP ≫ dATP > dTTP > dGTP (Figure 4), a preference that is identical to the earlier results conducted at 37°C with a longer DNA substrate (Brown *et al*, 2008). These results are consistent with the structures in which the replicative base pair is either in a WC base pair (GG2) or in a misaligned WC base pair with a strong and symmetric H-bond (GG1). Interestingly, the dCTP misincorporation appears more pronounced than other dNTP misincorporations in Pt-GG adducted DNA replication (Figure 4, right panels). The dCTP mismatches are shown as a strong band in the extension (Figure 4C) and extra bands after two insertions

(Figure 4A and B). The pronounced C base mismatches are likely associated with the unstable replicating base pairs in the lesion DNA structures, which increases the probability of template-primer misalignment. Template-primer misalignment is sequence dependent (Ling *et al*, 2004a; Garcia-Diaz and Kunkel, 2006; Bauer *et al*, 2007), thus, a two G base lesion, such as Pt-GG, in the template may promote pronounced C misincorporation specifically.

Earlier kinetic studies have suggested that two distinct populations appear during nucleotide incorporation against the 3'G and 5'G of the Pt-GG lesion by Dpo4 (Brown *et al*, 2008). We confirmed that two distinct kinetic populations also existed with Dpo4 by performing similar kinetic assays with short primer-template DNA at room temperature (data not shown). Biphasic kinetics is consistent with the multiple conformations and mobility of the DNA substrate observed in the GG1 and GG2 structures.

In vivo studies of Pt-GG bypass

TLS by the human Y-family enzymes is a putative mechanism of intrinsic cisplatin resistance (Rabik and Dolan, 2007). However, the overlapping functions among the 16 human DNA polymerases complicate the contribution by Y-family DNA polymerases (Shachar *et al*, 2009). *S. solfataricus* is an ideal model organism, as it encodes only one Y-family DNA polymerase, Dpo4, which has TLS function *in vitro*. To better understand how a Y-family enzyme participates in the mechanism of drug resistance, we constructed a *dpo-4* knockout mutant of *S. solfataricus* by targeted gene disruption as described earlier (Worthington *et al*, 2003; Schelert *et al*, 2004) and characterized the consequence of Dpo4 deficiency. The *dpo-4* chromosomal mutation was confirmed using PCR to show that the mutant strain carried a disrupted *dpo-4* allele due to *lacS* gene insertion; and by western blot analysis to show the absence of detectable levels of Dpo4 in cell extracts (Supplementary Figures S5 and S6). Physiological studies that compared the *dpo-4* mutant with its otherwise isogenic wild-type parent were conducted and showed that Dpo4 was not essential for life as the growth rate, cell yield, efficiency of plating, and cell morphology were all normal in the *dpo-4* mutant strain (data not shown). These data also indicate that Dpo4 did not contribute substantially to replicative synthesis of the chromosome. However, chemical challenge using cisplatin reveals that Dpo4 deficiency elicited significant biological effects. To directly evaluate the *in vivo* function of Dpo4 towards cisplatin, a dose-response study was conducted using both the wild-type and *dpo-4* disruption mutant cell lines. The 50% lethal concentration (LC_{50}) values of cisplatin were 23 µg/ml for the wild-type and 16 µg/ml for the *dpo-4* mutant (Supplementary Figure S7). The reduction in LC_{50} dose of cisplatin in the *dpo-4* strain shows that Dpo4 has a significant function in the tolerance of cisplatin. Proteomic analysis revealed that Dpo4 deficiency perturbed the abundance of many proteins (Figure 5; Supplementary Table S2). For example, proteins with increased abundance in the *dpo-4* mutant include peptidyl-prolyl isomerase (SSO0758), fibrillarin (SSO0940), and single-stranded DNA binding protein (SSO2364). Together, increased abundance of these proteins suggests that Dpo4 deficiency elicits some form of genomic stress and is consistent with heightened sensitivity to cisplatin drug challenge.
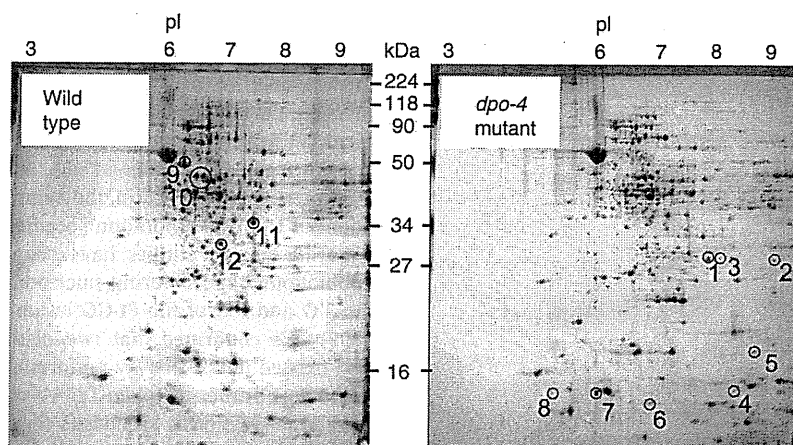
Figure 5 Analysis of wild-type and *dpo-4* mutant proteomes. Proteins from cell extracts prepared from exponentially growing cell lines, were fractionated by 2D SDS–PAGE and their identities were determined by tandem MS/MS sequencing of peptides derived by trypsin hydrolysis, with subsequent matching to the *S. solfataricus* genome sequence. Values for isoelectric point (pI) and mass (MW) are indicated across the top and sides of the figure, respectively. Proteins with increased abundance in the *dpo-4* mutant are circled in the *dpo-4* panel; proteins with decreased abundance are circled in the wild-type panel. Proteins are numbered in correspondence with Supplementary Table S2.

Discussion

Structural snapshots capture unique Pt-GG conformational transitions in an active Y-family polymerase

Our structures provide the first complete picture of how a Y-family DNA polymerase traverses the two G bases of a Pt-GG cross-link and catalyses primer extension beyond the damaged site. The adduct in the template strand is shown in three distinct positions relative to the incoming nucleotide at the active site, clearly illustrating the translocation of the lesion template during bypass. Particularly, all three DNA-bound Dpo4 structures are in a common closed conformation in which the finger, thumb, and little finger domains grip DNA tightly (Ling et al, 2001; Nair et al, 2006; Lone et al, 2007; Kirouac and Ling, 2009). Interestingly, Pt-GG undergoes significant conformational changes, as it travels through the active site from GG1 to GG3. With the conformational change, the 5'G base of Pt-GG is able to enter into the active site in GG2 and GG3, which have the entire double-base adduct accommodated in a straight DNA helix. The unique conformational change of Pt-GG is not observed in the earlier ypolη structures (Figure 2F) (Alt et al, 2007). The second insertion ypolη structure with dATP does not translocate the 5'G into its active site and keeps the Pt-GG adduct in similar conformations and positions in both insertion stages (Figure 2F). In addition, our structures with an extension stage further highlight the importance of the depressed Pt-GG conformation to the DNA helix in the productive ternary complexes after the first insertion.

Unique mechanism for double-base lesion bypass

The Pt-GG bypass differs from the only other double-base bypass in complex with Dpo4 for the *cis-syn* cyclobutane pyrimidine dimer lesion (CPD, TT dimer). For CPD lesion bypass, the entire TT dimer enters Dpo4's active site during the two-stage bypass, without conformational changes occurring in the dimer (Ling et al, 2003). The rigid and compact nature of the CPD allows Dpo4 to accommodate the entire

double-base lesion in the active site for both insertion stages. In Pt-GG bypass, Dpo4 has to alter the conformation of the adduct to accommodate the Pt-GG adduct in its active site. The structural differences reflect the varying catalytic efficiencies of Dpo4 bypassing different double-base lesions at the two insertion stages. Dpo4 bypasses the 5'T (second insertion) more efficiently than the 3'T (first insertion) because the double-base lesion does not fit the 'closed off' the active site well at the first insertion stage (Ling et al, 2003). In contrast, the insertion efficiency at the second insertion in Pt-GG bypass is much lower (180-fold) than the first insertion (Brown et al, 2008). The structural basis for lower dCTP incorporation against the 5'G at the second insertion would be strong geometric strains on the adduct when the angular adduct moves into the active site and the translocation-coupled conformational conversion, which is likely to be entropically costly. Thus, TLS for different double-base lesions catalysed by the same enzyme occurs through different bypass mechanisms, as revealed by the structural analyses.

Of the human Y-family enzymes, polη bypasses cisplatin-DNA adducts error freely while polκ performs error-prone TLS across Pt-GG (Bassett et al, 2003; Shachar et al, 2009). Human polκ keeps a similar closed conformation on the finger domain as Dpo4 and other mammalian Y-family polymerases (Supplementary Figure S2). A polη structure is only available from the yeast homologue (Alt et al, 2007), in which the finger domain is 16° open from the common closed conformation. The open conformation of ypolη seems unable to translocate the Pt-GG adduct within the active site (Figure 1D). Moreover, based on steady-state kinetic data, the extension step for hpolη is more difficult than Dpo4 in the incorporation opposite the lesion (Bassett et al, 2003), which is different from Dpo4 that has lowest replication efficiency at the second insertion. This discrepancy may be caused by structural differences observed in the two polymerases. The open conformation of ypolη does not confine the entire adduct into the active site (Alt et al, 2007), which may affect the extension step. A recent study suggested that multiple polymerases participate in the bypass of Pt-GG in mammalian